Draft version June 2, 2025
Typeset using LaTeX **twocolumn** style in AASTeX631

Challenges to the Two-Infall Scenario by Large Stellar Age Catalogs

Liam O. Dubay[1,2], Jennifer A. Johnson[1,2], James W. Johnson[3] and John D. Roberts[1,2]

[1] *Department of Astronomy, The Ohio State University, 140 W. 18th Ave, Columbus OH 43210, USA*
[2] *Center for Cosmology and AstroParticle Physics, The Ohio State University, 191 W. Woodruff Ave., Columbus OH 43210, USA*
[3] *Observatories of the Carnegie Institution for Science, 813 Santa Barbara St., Pasadena CA 91101, USA*

ABSTRACT

Stars in the Milky Way disk exhibit a clear separation into two chemically distinct populations by their [α/Fe] ratios. This α-bimodality is not a universal feature of simulated disk galaxies and may point to the Milky Way's unique evolutionary history. A popular explanation is the two-infall scenario, which postulates that two periods of substantial accretion rates dominate the assembly history of the Galaxy. However, most previous studies using the two-infall scenario have explored a limited portion of the parameter space, typically neglecting radial migration and assuming that the Galactic disk never ejected a substantial outflow. Thanks to advances in stellar age measurements in recent years, we can now also compare this popular model to more direct measurements of the Galaxy's evolutionary timescales across the disk from large stellar catalogs. We run multi-zone galactic chemical evolution (GCE) models with a two-infall-driven star formation history, radially dependent mass-loaded outflows, and a prescription for radial migration tuned to a hydrodynamical simulation. We compare our model results to abundance patterns across the disk from APOGEE DR17, supplemented with stellar age estimates through multiple methods. Although the two-infall scenario offers a natural explanation for the [α/Fe] bimodality, it struggles to explain several features of the age–abundance structure in the disk. The two-infall scenario generically predicts a massive and long-lasting dilution event, but the data show that stellar metallicity is remarkably constant with age across much of the Galactic disk. This apparent age-independence places considerable restrictions upon the two-infall parameter space. These issues can be mitigated, but not completely resolved, by allowing the accreted gas to be pre-enriched to low metallicity. Additionally, the two-infall scenario predicts that local metal-rich stars should have a bimodal distribution of ages, whereas APOGEE data show most of these stars have intermediate ages. Restrictions upon the two-infall parameter space also limit the application of other merger-dominated star formation histories to the Milky Way.

1. INTRODUCTION

Galactic chemical evolution (GCE) studies aim to explain the observed stellar abundance patterns in the Milky Way (MW) by modeling the star formation history and evolution of the Galaxy. A long-standing paradigm of GCE is that the metallicity of the interstellar medium (ISM) increases over time due to supernova enrichment from successive generations of stars (e.g., Tinsley 1979; Matteucci & Greggio 1986). In this view, one feature of the MW disk that is difficult to explain is the so-called "α-bimodality": the presence of two populations of stars at similar metallicity but separated by their [α/Fe] ratio (e.g., Bensby et al. 2014). The high-α sequence consists of old stars ($\gtrsim$ 9 Gyr; e.g., Pinsonneault et al. 2025) with super-Solar [α/Fe] and is associated with the kinematic thick disk (e.g., Fuhrmann 1998), while the low-α sequence is younger, with approximately Solar [α/Fe], and is associated with the thin disk. The α-bimodality is present across the Galactic disk, but the relative strength of the high- and low-α sequences varies by location (Hayden et al. 2015).

An explanation for the MW α-bimodality has yet to be broadly accepted in the GCE literature. An α-bimodality is not a universal feature in simulated MW-mass galaxies (e.g., Mackereth et al. 2018; Parul et al. 2025), and seems to not exist in M31 (Nidever et al. 2024; but see also Kobayashi et al. 2023), so its presence and characteristics in our Galaxy may provide clues

Corresponding author: Liam O. Dubay
dubay.11@osu.edu

to its unique evolutionary history. GCE models that attempt to solve this problem generally fall into two camps. Some explain the α-bimodality as a result of secular processes, such as the radial migration of stars and the inside-out growth of the disk (e.g., Kubryk et al. 2015; Sharma et al. 2021; Chen et al. 2023; Prantzos et al. 2023). Others argue for a bursty star formation history, perhaps driven by multiple accretion events (e.g., Chiappini et al. 1997; Mackereth et al. 2018; Spitoni et al. 2023) or a change in the star formation efficiency (Conroy et al. 2022).

The two-infall model of chemical evolution was proposed by Chiappini et al. (1997) to explain the origin of the high- and low-α disks. Though the model has been revised and refined since, the basic premise remains the same: the rate of gas infall onto the Galaxy is described by two consecutive, exponentially declining bursts. The relatively low infall rate between the two bursts leads to a lower star formation rate, allowing the gas abundance to evolve between the high- and low-α sequences while producing few stars in between. The infall timescale for the low-α disk can be varied to produce inside-out disk growth and a radial metallicity gradient (Romano et al. 2000). The initial model of Chiappini et al. (1997) successfully reproduced the available abundance data at the time, which were largely confined to the Solar neighborhood.

Subsequent studies refined the two-infall model to reproduce abundance data across the disk (e.g., Chiappini et al. 2001, 2003). Others have explored the SN Ia delay-time distribution (Matteucci et al. 2009; Palicio et al. 2023), galactic fountains (Spitoni et al. 2009), radial gas flows (Spitoni & Matteucci 2011; Palla et al. 2020), a variable star formation efficiency (Spitoni & Matteucci 2011; Palla et al. 2020), radial stellar migration (Spitoni et al. 2015; Palla et al. 2022), azimuthal abundance variations due to spiral modes (Spitoni et al. 2019), and pre-enriched gas infall (Palla et al. 2020; Spitoni et al. 2024) in a two-infall context. Recently, Spitoni et al. (2023) and Palla et al. (2024) proposed a third gas accretion event in the last ~ 3 Gyr to match the inferred star formation history from *Gaia* (Ruiz-Lara et al. 2020) and explain the recent abundance evolution of the Solar neighborhood.

Most previous studies of the two-infall model have not included mass-loaded outflows. Some hydrodynamic simulations of Galactic fountains ejected by CC SNe have shown that ejected material falls back onto the disk on relatively short timescales (Spitoni et al. 2008, 2009) and close to their point of origin (Melioli et al. 2008, 2009), suggesting the effect on GCE could be minimal. However, the effects of feedback in simulations are sensitive to its implementation (e.g., Li et al. 2020; Hu et al. 2023), and other simulations of MW-like galaxies with different feedback prescriptions do produce mass-loaded outflows (e.g., Brook et al. 2011; Gutcke et al. 2017; Nelson et al. 2019; Peschken et al. 2021; Kopenhafer et al. 2023). Empirically, mass-loaded outflows have been observed in nearby starburst galaxies (e.g., Lopez et al. 2020; Cameron et al. 2021; Lopez et al. 2023) but not MW-like systems, although the predicted column densities are below current detection limits (see reviews by Veilleux et al. 2020; Thompson & Heckman 2024). Even if the MW is not currently ejecting a substantial outflow, it is not unreasonable to suppose that it may have during a more active phase in its evolutionary history.

By neglecting Galactic outflows, previous studies of the two-infall scenario have been constrained in their choice of nucleosynthetic yields (François et al. 2004) because of the yield–outflow degeneracy. Weinberg et al. (2017) showed that the equilibrium metallicity is primarily set by the yields and outflow mass-loading factor; proportionally raising or lowering both may affect the path of chemical evolution but not the end-point. This degeneracy prohibits direct estimates of the yield scale from GCE models, unless the effect of outflows is assumed to be insignificant (e.g., François et al. 2004). The predicted yields from CCSN models can vary substantially depending on the choice of initial mass function (Vincenzo et al. 2016) and the physics of black hole formation (Griffith et al. 2021), yet few studies have investigated the effect of the yield scale on two-infall scenario predictions. Varying the yield scale while maintaining an evolutionary end point that is consistent with observations requires flexibility in the strength of outflows.

The two-infall model attempts to reproduce the full distribution of stellar abundances in the Solar neighborhood through a single, continuous evolutionary track. However, the current body of evidence suggests that many of the stars that make up the wings of the local metallicity distribution originate from elsewhere in the Galaxy. Sellwood & Binney (2002) first showed that transient spiral perturbations can induce large changes in the guiding radius of a star without kinematic heating, and it is now understood that the stars that make up the Solar neighborhood are drawn from a wide range of birth radii (e.g., Schönrich & Binney 2009; Frankel et al. 2018; Lehmann et al. 2024). Some studies have attempted to derive stellar birth radii (e.g., Ratcliffe et al. 2023; Lu et al. 2024), though such an endeavor requires also reconstructing the evolution of the Milky Way's radial metallicity gradient. While the strength and speed of radial migration in the disk are not precisely measured, it is clear that a single chemical evolution track need not explain the entirety of the local observed abundance distribution.

The chemical and kinematic separation of the high- and low-α disks remains the primary observational evidence behind the two-infall model. Spitoni et al. (2024) argued that the observed gap between the sequences in [α/Fe], contrasted with their overlap in [α/H], indicates a period of reduced star formation, which is a natural consequence of the two-infall model. In different samples, Nissen et al. (2020) and Nataf et al. (2024) observed multiple sequences in the local age–metallicity relation, which would naturally be explained by the two-infall scenario. Many two-infall studies have also reproduced the metallicity gradient, the local surface densities of stars and gas, and the local star formation and supernova rates (e.g., Chiappini et al. 1997; Romano et al. 2000; Spitoni et al. 2024), although the ability to match these observables is not unique to the two-infall scenario.

In contrast to the two-infall scenario, a number of studies have attempted to explain the α-bimodality through purely secular processes. Using a detailed prescription for radial migration, Schönrich & Binney (2009) produced distinct high- and low-α sequences, but they did not overlap in metallicity space as would be found by later surveys (e.g., Bensby et al. 2014). Others have produced a more MW-like α-bimdodality using a combination of radial migration and inside-out galaxy growth (e.g., Kubryk et al. 2015; Sharma et al. 2021; Chen et al. 2023; Prantzos et al. 2023). In this scenario, the local high-α population originates from the inner Galaxy, where the star formation rate peaked early in its history. Sharma et al. (2021) and Chen et al. (2023) suggest that a simultaneous decline in the star formation rate and the [α/Fe] ratio is needed to separate the sequences in chemical space. Chen & Prantzos (2025) additionally argue that the double sequence in the local age–metallicity relation observed by Nissen et al. (2020) can also be explained by smooth star formation with inside-out growth. On the other hand, some GCE models that incorporate both radial migration and smooth, inside-out star formation have failed to produce an α-bimodality (e.g., Johnson et al. 2021; Dubay et al. 2024). While the α-bimodality remains a key piece of evidence for the two-infall scenario, it has been reproduced by other models.

As stellar age estimation techniques have improved over recent years, large catalogs have become available with ages for hundreds of thousands or even millions of stars from a wide swath of the Galaxy. In a challenge to the traditional view of GCE, which expects the ISM metallicity to continually increase over time, Johnson et al. (2024) examined the age–metallicity relation at different radii from the astroNN catalog (Mackereth et al. 2019) and found that the mode of the metallicity distribution at a given radius is nearly independent from age over the past $\sim 9\,\mathrm{Gyr}$. They propose an "equilibrium scenario" in which the local metallicity is driven by the ratio of star formation to accretion at a given radius, which evolves to a constant over $\sim$ Gyr timescales. Whether the equilibrium metallicity is regulated by outflows, as proposed by Johnson et al. (2024), or by other factors such as a radial gas flow, the current data suggest that the gas abundance across the Galaxy has evolved very little over most of the thin disk lifetime.

In light of the findings of Johnson et al. (2024) and a new empirical yield scale from Weinberg et al. (2024), we evaluate the predictions of the two-infall model against stellar age and abundance data across the MW disk. We run multi-zone GCE models with a two-infall accretion history, radially-dependent mass-loaded outflows, and a prescription for radial migration tuned to a hydrodynamical simulation. We investigate the impact of the scale of SN yields and outflows, the strength of radial migration, the enrichment of the circumgalactic medium, and the local disk mass surface density ratio on the GCE model predictions. We compare our results to abundance distributions across the disk from APOGEE DR17, and to age–abundance relations from multiple age catalogs. We describe our observational sample in Section 2, and we detail our chemical evolution models and parameter selection in Section 3. We compare our multi-zone model predictions to the data in Section 4. We discuss our results in Section 5 and summarize our conclusions in Section 6.

2. OBSERVATIONAL SAMPLE

We compare our models against stellar abundances from the Apache Point Observatory Galactic Evolution Experiment (APOGEE; Majewski et al. 2017) data release 17 (DR17; Abdurro'uf et al. 2022). APOGEE data were obtained from infrared spectrographs (Wilson et al. 2019) mounted on the 2.5-meter Sloan Foundation Telescope (Gunn et al. 2006) at Apache Point Observatory and the Irénée DuPont Telescope (Bowen & Vaughan 1973) at Las Campanas Observatory. The data reduction pipeline is described by Nidever et al. (2015), and APOGEE Stellar Parameter and Chemical Abundance Pipeline (ASPCAP) is detailed by Holtzman et al. (2015), García Pérez et al. (2016), and Jönsson et al. (2020).

We obtain a sample of 171 635 red giant branch and red clump stars with high-quality spectra using the selection criteria listed in Table 1, which are adapted from

Table 1. Sample selection parameters from APOGEE DR17 (see Section 2).

Parameter	Range or Value	Notes
$\log g$	$1.0 < \log g < 3.8$	Select giants only
$T_{\rm eff}$	$3500 < T_{\rm eff} < 5500$ K	Reliable temperature range
S/N	$S/N > 80$	Required for accurate stellar parameters
ASPCAPFLAG Bits	$\notin$ 23	Remove stars flagged as bad
EXTRATARG Bits	$\notin$ 0, 1, 2, 3, or 4	Select main red star sample only
NN age error	$\sigma_\tau/\tau < 40\%$	Age uncertainty from Leung et al. (2023)
$R_{\rm gal}$	$3 < R_{\rm gal} < 15$ kpc	Eliminate bulge & extreme outer-disk stars
$\lvert z\rvert$	$\lvert z\rvert < 2$ kpc	Eliminate halo stars

Table 2. Median and dispersion in APOGEE parameter uncertainties.

Parameter	Median Uncertainty	Uncertainty Dispersion (95% − 5%)
[O/H]	0.019	0.031
[Fe/H]	0.0089	0.0060
$\log_{10}(\tau_{\rm NN}/{\rm Gyr})$	0.10	0.16
$\tau_{\rm [C/N]}/{\rm Gyr}$	1.4	1.8

Hayden et al. (2015). Table 2 presents the median statistical uncertainty and uncertainty dispersion ($95^{\rm th} - 5^{\rm th}$ percentile difference) of the calibrated [Fe/H] and [O/Fe] abundances for our sample. When calculating the galactocentric radius $R_{\rm gal}$ and midplane distance z of each star, we use the Bailer-Jones et al. (2021) photogeometric distance estimates from *Gaia* Early Data Release 3 (Gaia Collaboration et al. 2016, 2021) included in the APOGEE DR17 catalog and we adopt the Galactic coordinates of the Sun $(R, z)_\odot = (8.122, 0.0208)$ kpc (GRAVITY Collaboration et al. 2018; Bennett & Bovy 2019).

2.1. *Stellar Age Estimates*

We supplement the APOGEE DR17 abundance data with two different age catalogs. The first is from Leung et al. (2023), who train a variational encoder-decoder network on asteroseismic data for APOGEE red giants with $2.5 < \log g < 3.6$. This catalog has two main advantages over other neural network (NN) age estimates: their method is designed to reduce contamination from abundance information (in particular [α/Fe]), and the recovered ages do not plateau at ~ 10 Gyr as they do in some other neural network-derived age catalogs (e.g., Mackereth et al. 2019). Following the recommendations of Leung et al. (2023), we cut all stars which have a relative age uncertainty greater than 40%. This produces a sample of 57 607 stars with NN age estimates, of which 14 871 are in the Solar neighborhood ($7 \leq R_{\rm gal} < 9$ kpc, $0 \leq |z| < 0.5$ kpc). The median uncertainty in log-age is 0.10 (see Table 2).

Our second age catalog utilizes the [C/N]–age relation calibrated by Roberts et al. (in prep) for red giant branch (RGB) and red clump stars. The relationship relies on the mass-dependent level of mixing during the first dredge-up (FDU; Iben 1967) to map the correlation of stellar mass, and hence age, with surface chemistry. This method has the benefit of providing age estimates for luminous giants ($\log g < 2.5$), which increases the sample size at larger distances from the Sun. However, limitations from the efficiency of FDU mixing and the RGB age–mass relationship mean the ages are not trustworthy outside the range $1 \sim 10$ Gyr. Additional mixing effects in low-metallicity stars also prevent the relation from being applied to luminous giant and red clump stars with [Fe/H] < -0.4. The median propagated uncertainty for the [C/N]-derived ages is ~ 1 Gyr; however, as noted by Roberts et al. (in prep), the propagated errors underestimate the true age dispersion, so we enhance the uncertainties by 40% (see Table 2). With this relationship, we estimate ages for 113 464 stars across the disk, including 20 995 in the Solar neighborhood.

3. CHEMICAL EVOLUTION MODELS & PARAMETER SELECTION

We run multi-zone GCE models using the Versatile Integrator for Chemical Evolution (`VICE`; Johnson & Weinberg 2020). The basic format of our models follows Johnson et al. (2021) and Dubay et al. (2024). We set up a disk with radial extent $0 \leq R_{\rm gal} < 20$ kpc that is divided into concentric rings of width $\delta R_{\rm gal} = 100$ pc. We use a time-step size of $\Delta t = 10$ Myr and a resolution of $n = 8$ stellar populations per time-step per ring, and we run our models up to a final time of $t_{\rm final} = 13.2$ Gyr.

Within each ring, chemical evolution proceeds according to a conventional one-zone GCE model with instantaneous mixing and continuous recycling. Stellar populations migrate between zones as described in Section 3.6, allowing the long-lived progenitors of SNe Ia to enrich areas of the Galaxy outside of their birth zones. We inhibit star formation past $R_{\rm gal} > 15.5$ kpc, so stars in the outer 4.5 kpc of the model disk represent a purely migrated population. We also assign a final midplane distance to each stellar population as described in Section 3.6. We do not incorporate radial gas flows between the different zones, but we discuss their potential implications in Section 5.4.

We discuss our assumptions about the nucleosynthetic yields in Section 3.1, the outflow prescription in Section 3.2, the gas supply in Section 3.3, the infall parameter selection in Section 3.4, the star formation law in Section 3.5, and the stellar migration prescription in Section 3.6. Table 3 summarizes the most relevant variables and their fiducial values in this work.

3.1. *Nucleosynthetic Yields*

The population-averaged nucleosynthetic yields of CCSNe, $y_{\rm X}^{\rm CC}$, are uncertain to a degree that is significant for chemical evolution models. This problem is exacerbated by the complexity of the CCSN explosion landscape (Sukhbold et al. 2016). Recently, Weinberg et al. (2024) used a measurement of the mean Fe yield of CC SNe by Rodríguez et al. (2023) and the plateau in stellar [α/Fe] abundances at low metallicity to infer population-averaged yields of $y/Z_\odot \approx 1$—in other words, for every $1\,{\rm M}_\odot$ of stars formed, massive stars release a mass of newly-synthesized α-elements (e.g., O or Mg) equal to their mass in the Sun. However, Johnson et al. (2024) found that GCE models with yields at this scale approach present-day abundances too slowly to match the observed age–metallicity relation. Previous multi-zone models using `VICE` (e.g., Johnson et al. 2021; Dubay et al. 2024) adopted higher yields ($y/Z_\odot \approx 2.6$) based on Chieffi & Limongi (2004) and Limongi & Chieffi (2006); however, in order to produce a realistic evolution of [O/Fe], those studies adopted an integrated SN Ia rate which is high compared to the measurement of Maoz & Graur (2017).

We investigate yield sets at multiple scales of the Solar abundance. The CCSN yield of O is directly set by the Solar scale, $y_{\rm O}^{\rm CC} = (y/Z_\odot)Z_{{\rm O},\odot}$, because all O is assumed to form in CCSNe. For Fe, the CCSN yield is set by the [α/Fe] "plateau" at low metallicity, $[\alpha/{\rm Fe}]_{\rm CC}$, such that $y_{\rm Fe}^{\rm CC} = (y/Z_\odot)Z_{{\rm Fe},\odot}10^{-[\alpha/{\rm Fe}]}$ (for further discussion on the empirical yield scale and the CCSN plateau, see Weinberg et al. 2024). We adopt the Asplund et al. (2009) Solar abundances: $Z_{{\rm O},\odot} = 5.72 \times 10^{-3}$ and $Z_{{\rm Fe},\odot} = 1.29 \times 10^{-3}$. Our yield sets are presented in Table 4. We consider $y/Z_\odot = 1$ representative of the empirical yield scale, whereas $y/Z_\odot = 2 - 3$ span a range of theoretical predictions.

The SN Ia yield of Fe, $y_{\rm Fe}^{\rm Ia}$, is set so that our models reach [O/Fe] ≈ 0.0 by $t = 13.2$ Gyr. For $y/Z_\odot = 3$, the combined Fe yield of CCSNe and SNe Ia matches the Solar yield scale: $(y_{\rm Fe}^{\rm Ia} + y_{\rm Fe}^{\rm CC})/Z_{{\rm Fe},\odot} = y/Z_\odot$; for $y/Z_\odot = 1$ and $y/Z_\odot = 2$, we enhance $y_{\rm Fe}^{\rm Ia}$ by a factor of 30% and 10%, respectively, to reach the desired endpoint. The fifth row of Table 4 reports the integrated SN Ia rate

$$\frac{N_{\rm Ia}}{M_\star} = \frac{y_{\rm Fe}^{\rm Ia}}{\bar{m}_{\rm Fe}^{\rm Ia}} \tag{1}$$

from each yield set, assuming a mean Fe yield per SN Ia of $\overline{m}_{\rm Fe}^{\rm Ia} = 0.7$ M$_\odot$ (Mazzali et al. 2007; Howell et al. 2009). The rate for the $y/Z_\odot = 1$ yield set is slightly higher than the volumetric rate of $N_{\rm Ia}/M_\star = (1.3{\pm}0.1)\times10^{-3}\,{\rm M}_\odot^{-1}$ reported by Maoz & Graur (2017), but is consistent with their measurement of $N_{\rm Ia}/M_\star = (1.6 \pm 0.3) \times 10^{-3}\,{\rm M}_\odot^{-1}$ for field galaxies. The rate for the $y/Z_\odot = 2$ yield set is consistent with the measurement of $N_{\rm Ia}/M_\star = (2.2 \pm 1.0) \times 10^{-3}\,{\rm M}_\odot^{-1}$ by Maoz & Mannucci (2012), while the rate for the $y/Z_\odot = 3$ yield set is generally higher than literature values.

Unlike CCSNe, SNe Ia populate a broad distribution of delay times between progenitor formation and explosion. The time-dependent SN Ia rate in units of ${\rm M}_\odot^{-1}\,{\rm yr}^{-1}$ is defined as

$$R_{\rm Ia}(t) = \begin{cases} \frac{N_{\rm Ia}}{M_\star}\frac{f_{\rm Ia}(t)}{\int_{t_D}^{t_{\rm max}} f_{\rm Ia}(t')dt'}, & t \geq t_D \\ 0 & t < t_D, \end{cases} \tag{2}$$

where $t_D = 40$ Myr is the minimum SN Ia delay time, $t_{\rm max} = 13.2$ Gyr is the lifetime of the disk, $N_{\rm Ia}/M_\star$ is the total number of SNe Ia per unit mass of star formation, and $f_{\rm Ia}(t)$ is the un-normalized form of the DTD. Motivated by the finding by Dubay et al. (2024) that a large fraction of long-delayed SNe Ia improves agreement with the Milky Way's high-α sequence, we adopt a wide plateau DTD of the form

$$f_{\rm Ia}(t) = \begin{cases} 1, & t < 1\,{\rm Gyr} \\ (t/1\,{\rm Gyr})^{-1.1}, & t \geq 1\,{\rm Gyr}. \end{cases} \tag{3}$$

We discuss the implications of using a different DTD in Section 4.3.

Many previous two-infall studies have adopted the yields of François et al. (2004), who in turn adapted

Table 3. A summary of variables and their fiducial values for our chemical evolution models (see discussion in Section 3).

Quantity	Fiducial Value	Alternatives	Section	Description
$y/Z_\odot$	1	2, 3	3.1	Scale of nucleosynthetic yields (see Table 4)
$f_{\rm Ia}(t)$	Equation 3	Equation 15	3.1	Delay-time distribution of Type Ia supernovae
$\eta_\odot$	0.2	1.4, 2.4	3.2	Outflow mass-loading factor at $R_\odot$ (see Table 4)
R_η	5.0 kpc	—	3.2	Exponential outflow scale radius
$f_\Sigma(R_\odot)$	0.12	0.25, 0.5	3.3	Local thick/thin disk surface density ratio
$[{\rm X/H}]_{\rm CGM}$	Pristine	-0.7, -0.5	3.3	Metallicity of infalling gas
τ_1	1 Gyr	$0.1-3$ Gyr	3.4	Timescale of the first infall epoch
$\tau_2(R_\odot)$	15 Gyr	$3-30$ Gyr	3.4	Timescale of the second infall epoch at the Solar annulus
R_{τ_2}	7 kpc	—	3.4	Exponential scale radius of the second infall timescale
$t_{\rm max}$	4.2 Gyr	$1-5$ Gyr	3.4	Time of maximum gas infall (onset of second infall)
$\sigma_{\rm RM8}$	2.68 kpc	3.6, 5.0 kpc	3.6	Radial migration strength

Table 4. Nucleosynthetic yields and outflow prescriptions.

	$y/Z_\odot = 1$ (empirical)	$y/Z_\odot = 2$ (theoretical)	$y/Z_\odot = 3$ (extreme)
$y_{\rm O}^{\rm CC}$	5.72×10^{-3}	1.14×10^{-2}	1.72×10^{-2}
$y_{\rm Fe}^{\rm CC}$	4.58×10^{-4}	9.15×10^{-4}	1.37×10^{-3}
$y_{\rm O}^{\rm Ia}$	0	0	0
$y_{\rm Fe}^{\rm Ia}$	1.08×10^{-3}	1.83×10^{-3}	2.50×10^{-3}
$N_{\rm Ia}/M_\star$ [$M_\odot^{-1}$]	1.55×10^{-3}	2.62×10^{-3}	3.57×10^{-3}
$\eta_\odot$	0.2	1.4	2.4

those of Woosley & Weaver (1995) for CCSNe and Iwamoto et al. (1999) for SNe Ia to provide a better fit between GCE models and local abundance data. Notably, the yields for O and Fe were left unchanged from the original studies. However, because Woosley & Weaver (1995) report gross yields without detailed initial abundances for their CCSN progenitors, and because François et al. (2004) do not provide population-averaged yields, it is difficult to make a comparison with our yield sets. Ultimately, François et al. (2004) report that their GCE models are insensitive to changes in the CCSN yield of O by a factor of 2, so we consider it reasonable to explore the full range of yields given in Table 4.

Figure 1 illustrates the effect of the yield scaling on the abundance evolution in one-zone models. We vary the outflow mass-loading factor η for each model to achieve a consistent endpoint to the abundance evolution (see Section 3.2 for further discussion on outflows). All models feature a rapid dilution of the ISM metallicity by $\sim 0.5-0.8$ dex, visible in the top two panels, brought on by the infall of pristine gas at $t_{\rm max}$. For the model with $y/Z_\odot = 1$, this dilution persists for some time and the metallicity does not return to Solar until the close to present day. The models with higher yields and outflows recover from this dilution more quickly, returning to Solar metallicity by ~ 5 Gyr ago. However, the high-yield models experience a decline in [O/Fe] of ~ 0.2 dex between the second infall and the present day, contrasted with the smaller decline of ~ 0.1 dex in the low-yield model.

Figure 1 also indicates the mode of the APOGEE abundance distributions in 1 Gyr-wide age bins. As explained by Johnson et al. (2024), the mode is expected to be less sensitive to the effects of radial migration than other statistical measures. The data show that the evolution in [O/H] is close to flat over the past 5 Gyr. The behavior of the $y/Z_\odot = 2$ and $y/Z_\odot = 3$ models closely matches this trend in the data, whereas the $y/Z_\odot = 1$ model increases significantly by ~ 0.2 dex during the same time period. The [Fe/H] abundance in the data does increase slightly at late times, likely due to the delayed contribution of Fe from SNe Ia. Between lookback times of $\sim 5-9$ Gyr, the modes of [O/H] and [Fe/H] are higher than the present-day, likely due to a larger population of migrated stars relative to stars born in-situ at those times.

The three models in Figure 1 predict nearly identical evolution in [O/Fe] over the past 5 Gyr, and the trend in the data is similar apart from a ~ 0.05 dex offset (which could be corrected by increasing $y_{\rm Fe}^{\rm Ia}$ or adjusting the zero-point in the stellar abundances). The offset between the data and models grows between $\sim 5-8$ Gyr, especially for the higher yields. Of the three, the $y/Z_\odot = 2$ and $y/Z_\odot = 3$ models most closely match the observed late-time age–metallicity relations,

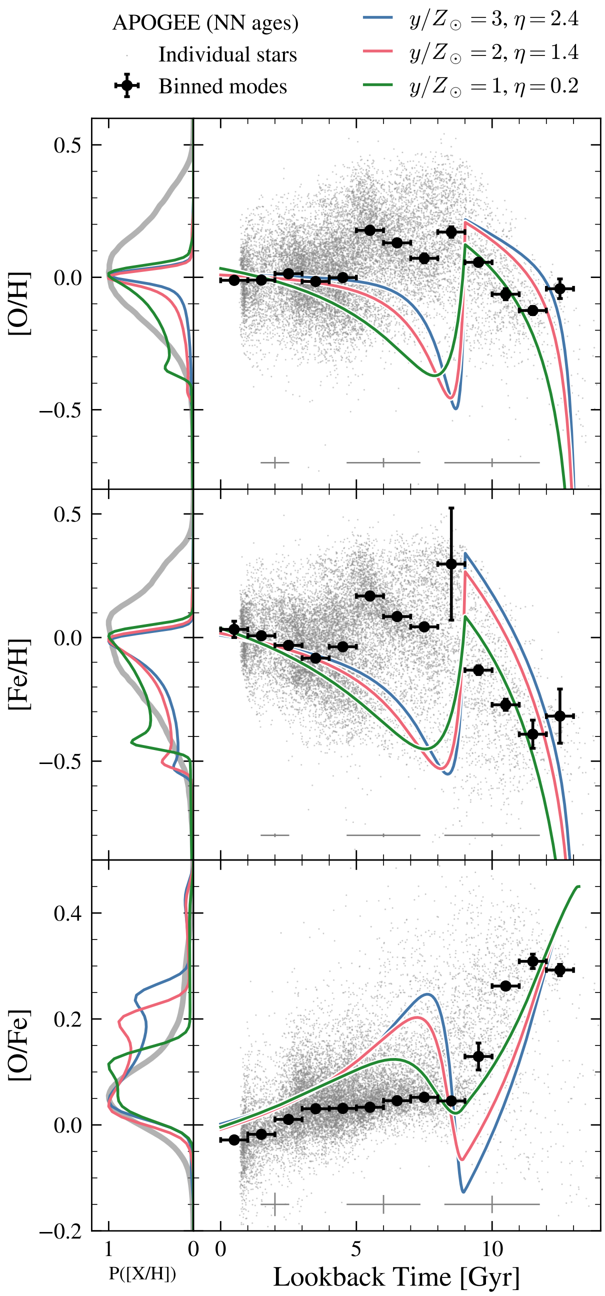

Figure 1. The abundance evolution of three one-zone models with different yield sets and outflow mass-loading factors. Table 4 presents the population-averaged yields for each model. The gray points plot the abundances of APOGEE stars with NN ages from Leung et al. (2023) from the Solar neighborhood ($7 \leq R_{\rm gal} < 9\,{\rm kpc}$, $0 \leq |z| < 0.5\,{\rm kpc}$). The black points with error bars indicate the mode of the abundance data in 1 Gyr-wide age bins, and the gray error bars along the bottom of each panel indicate the median age and abundance errors as a function of age.

whereas the $y/Z_\odot = 1$ model shows the best agreement with the observed [O/Fe] evolution. As the $y/Z_\odot = 2$ and $y/Z_\odot = 3$ models behave qualitatively similarly, we focus on the $y/Z_\odot = 1$ and $y/Z_\odot = 2$ yield sets for the remainder of this study.

3.2. *Outflows*

Mass-loaded outflows are a useful tool for scaling the endpoint of GCE models. Weinberg et al. (2017) showed that in the case of exponentially declining star formation, the O abundance approaches an equilibrium at

$$Z_{\rm O,eq} = \frac{y_{\rm O}^{\rm CC}}{1 + \eta - r - \tau_\star/\tau_{\rm SFH}}, \tag{4}$$

where $r = 0.4$ is the instantaneous recycling parameter, $\tau_\star$ is the star formation efficiency timescale, $\tau_{\rm SFH}$ is the star formation timescale, and $\eta \equiv \dot{\Sigma}_{\rm out}/\dot{\Sigma}_\star$ is the outflow mass-loading factor. Motivated by Equation 4, we adopt an outflow mass-loading factor at the Solar radius $\eta_\odot \equiv \eta(R = R_\odot)$ for each of the yield sets in Table 4. Models with lower yields do not achieve a steady-state abundance in time (see Figure 1); therefore, the values of $\eta_\odot$ for $y/Z_\odot = 1$ and $y/Z_\odot = 2$ are lower than would be suggested by Equation 4 in order to reach Solar metallicity at the end of the model.

Not all GCE studies have constrained their models to reach an equilibrium at the Solar metallicity. For example, the models of Palla et al. (2020) and Spitoni et al. (2024) predict somewhat super-Solar metallicity in the present-day Solar neighborhood. Measurements of gas-phase (e.g., Méndez-Delgado et al. 2022) and stellar abundances (Figure 1) indicate that the Solar neighborhood is presently close to Solar metallicity, so we use η to fine-tune the chemical evolution end-point to to $[{\rm O/H}] \approx 0.0$.

Equation 4 suggests that one can achieve a different $Z_{\rm O,eq}$ in different regions of the Galaxy by adopting a spatially-varying prescription for η. In order to produce an exponentially declining radial metallicity gradient, we adopt a prescription for the outflow mass-loading factor which increases exponentially with radius:

$$\eta(R_{\rm gal}) = \eta_\odot \exp\left(\frac{R_{\rm gal} - R_\odot}{R_\eta}\right) \tag{5}$$

where R_η is the exponential outflow scale radius and $R_\odot = 8\,{\rm kpc}$. As discussed by Johnson et al. (2024), an exponential trend in η with $R_{\rm gal}$ produces a linear trend in [O/H] with $R_{\rm gal}$. We adopt $R_\eta = 5$ kpc, a lower value than in Johnson et al. (2024), so that our $y/Z_\odot = 1$ model produces a radial abundance gradient of $\nabla[{\rm O/H}]_{\rm eq} \approx -0.06\,{\rm dex\,kpc^{-1}}$, in line with recent measurements from HII regions (Méndez-Delgado et al. 2022) and stars (Myers et al. 2022; Johnson et al. 2024).

Most previous studies of the two-infall model have assumed that the Milky Way has experienced no significant mass-loaded outflows. Even in studies which do incorporate Galactic winds, the mass-loading is relatively weak (e.g., $\eta \approx 0.2$ in Palicio et al. 2023). To achieve a realistic radial metallicity gradient, many studies have adopted the yields of François et al. (2004) and a prescription for the infall timescale of the thin disk that increases linearly with radius (e.g., Chiappini et al. 1997; Romano et al. 2000). Additionally, some studies have implemented radial gas flows or a variable star formation efficiency in order to regulate the radial metallicity gradient (e.g., Spitoni & Matteucci 2011; Palla et al. 2020).

As discussed by Johnson et al. (2024), evidence for or against outflows in Milky Way-type galaxies in simulations and observations is inconclusive. Because we aim to study the effect of the yield assumptions on two-infall model predictions, we use mass-loaded outflows to control the final state of chemical evolution across the disk. However, mass-loaded outflows are not a necessary ingredient for the results of this study. We find that a one-zone model with the fiducial parameters, $\eta = 0$, and $y/Z_\odot = 0.8$, predicts a similar abundance evolution and nearly identical stellar abundance distributions to the fiducial model with $\eta = 0.2$ and $y/Z_\odot = 1$.

3.3. *The Gas Supply*

We run `VICE` in "infall mode," where we specify the gas infall density $\dot{\Sigma}_{\rm in}$ and the star formation efficiency (SFE) timescale $\tau_\star \equiv \Sigma_g/\dot{\Sigma}_\star$ as functions of time. The gas surface density Σ_g and star formation rate $\dot{\Sigma}_\star$ are calculated from the two specified quantities according to our star formation law, which is described in Section 3.5, assuming zero initial gas mass in all zones.

The infall rate as a function of time and galactocentric radius can generically be described by

$$\dot{\Sigma}_{\rm in}(t, R_{\rm gal}) = A f_{\rm in}(t|R_{\rm gal}) g(R_{\rm gal}), \tag{6}$$

where $g(R_{\rm gal}) = \Sigma_\star(R_{\rm gal})/\Sigma_\star(R_{\rm gal} = 0)$ is the stellar density gradient, $f_{\rm in}$ is the infall rate over time, and A is the normalization. Because we incorporate mass-loaded outflows, A is not analytically solvable, so first we numerically integrate the star formation rate $\dot{\Sigma}_\star(t, R_{\rm gal})$ and then follow the procedure outlined in Appendix B of Johnson et al. (2021) to calculate A. The infall rate is normalized to produce a total disk stellar mass of $(5.17 \pm 1.11) \times 10^{10}\,{\rm M}_\odot$ (Licquia & Newman 2015) and to match the stellar surface density gradient of Bland-Hawthorn & Gerhard (2016).

The infall rate is described by two successive, exponentially declining bursts in time. The first infall component induces the formation of the thick disk, and the second component produces the thin disk. At a given galactocentric radius $R_{\rm gal}$, the un-normalized form of the infall rate is

$$f_{\rm in}(t|R_{\rm gal}) = e^{-t/\tau_1} + f_{2/1}(R_{\rm gal}) e^{-(t-t_{\rm max})/\tau_2}, \tag{7}$$

where τ_1 and τ_2 are the first and second infall timescales, respectively, $t_{\rm max}$ is the onset of the second infall and thus the time of maximum gas infall, and $f_{2/1}$ is the ratio of the second infall amplitude to the first. We numerically calculate $f_{2/1}$ for each zone such that the resulting stellar density profile follows a two-component disk, with the surface density ratio of the thick and thin disks given by

$$f_\Sigma(R) \equiv \frac{\Sigma_1(R)}{\Sigma_2(R)} = f_\Sigma(R_\odot) e^{(R-R_\odot)\cdot(1/R_2 - 1/R_1)}. \tag{8}$$

We adopt a thick disk scale radius of $R_1 = 2.0\,{\rm kpc}$, a thin disk scale radius of $R_2 = 2.5\,{\rm kpc}$, and a fiducial value for the local surface density ratio of $f_\Sigma(R_\odot) = 0.12$ (Bland-Hawthorn & Gerhard 2016).

The thick-to-thin disk density ratio is especially important for our GCE models as it controls the quantity of gas accreted during each infall epoch. Our fiducial value of $f_\Sigma(R_\odot) = 0.12$ is on the low end of literature estimates, which range from $f_\Sigma(R_\odot) \sim 0.06 - 0.6$ (e.g., Gilmore & Reid 1983; Siegel et al. 2002; Jurić et al. 2008; Mackereth et al. 2017; Fuhrmann et al. 2017). Previous two-infall studies have adopted a similarly broad range of values (e.g., $f_\Sigma(R_\odot) = 0.18$ from Spitoni et al. 2021; $f_\Sigma(R_\odot) = 0.4$ from Spitoni et al. 2024). We therefore explore values up to $f_\Sigma(R_\odot) = 0.5$ in our multi-zone models in Section 4.

In most of our models, we assume the infalling gas is pristine (i.e., $Z_{\rm in} = 0$). However, the circumgalactic medium (CGM) from which the infalling gas is drawn could be previously enriched, possibly from contributions from Galactic outflows, gas stripped from dwarf galaxies, or from SNe in the halo. The Milky Way's CGM is diffuse, multiphase, and inhomogeneous, making it difficult to study (e.g., Tumlinson et al. 2017; Mathur 2022); still, recent observations have confirmed the existence of metals at non-Solar abundance ratios in the CGM (e.g., Das et al. 2019, 2021; Gupta et al. 2021). We investigate models where the infalling gas is pre-enriched and its metallicity is described by

$$Z_{\rm in}(t) = (1 - e^{-t/\tau_{\rm rise}}) Z_\odot 10^{[{\rm X/H}]_{\rm CGM}}. \tag{9}$$

In this case, the metallicity rises from 0 with a timescale $\tau_{\rm rise} = 2\,{\rm Gyr}$ and plateaus at $[{\rm X/H}]_{\rm CGM} = [{\rm O/H}]_{\rm CGM} = [{\rm Fe/H}]_{\rm CGM}$. Previous GCE studies suggest that some level of enrichment of the infalling gas can improve agreement with observations (e.g., Palla et al. 2020; Johnson et al. 2024; Spitoni et al. 2024).

3.4. *Infall Rate Parameter Selection*

Previous studies have adopted a wide range of parameters for Equation 7. Figure 2 illustrates the effect of varying the infall parameters on gas abundance tracks and stellar abundance distributions in a one-zone model. The first infall timescale τ_1, shown in panel (a), primarily affects the stellar distribution along the high-α sequence. Though τ_1 has an apparently large effect on the size of the low-α loop, the effect on the stellar abundance distribution of the low-α sequence is quite small due to the low number of stars formed between $t \sim 3-6$ Gyr. We adopt $\tau_1 = 1$ Gyr for our fiducial value, in line with Spitoni et al. (2020) but longer than, e.g., Nissen et al. (2020) or Spitoni et al. (2021), in order to set the peak of the high-α sequence at [O/Fe] $\approx +0.3$.

Panel (b) of Figure 2 shows that the second infall timescale τ_2 controls the size of the low-α loop, which affects the width of the MDF and the low-α [O/Fe] distribution. A shorter τ_2 produces a bigger loop and therefore a broader [O/Fe] distribution which is skewed to higher [O/Fe], while a longer τ_2 produces a smaller loop, leading to both a narrower low-α sequence and a narrower MDF. We note that our maximum value of $\tau_2 = 30$ Gyr is close to a constant infall rate, so a further increase in τ_2 has diminishing returns. Between $\tau_2 = 3-30$ Gyr, the endpoint of the abundance tracks shifts by ~ 0.2 dex in [Fe/H] and ~ 0.1 dex in [O/Fe], which could affect the model's ability to reproduce the present-day abundance of the Solar neighborhood. We adopt a fiducial value of $\tau_2 = 15$ Gyr for the Solar neighborhood in order to minimize the size of the loop and width of the low-α [O/Fe] distribution while still approaching Solar [Fe/H] at late times (see further discussion in Section 4.3). This value is in line with the infall timescale recovered by Spitoni et al. (2020), and similar to the local star formation timescale adopted by Johnson et al. (2021), but significantly longer than the timescales found by Nissen et al. (2020) and Spitoni et al. (2021).

In our multi-zone models, we vary the second infall timescale with radius to produce inside-out growth of the disk. Previous multi-zone two-infall studies (e.g., Chiappini et al. 2001; Palla et al. 2020) scale τ_2 linearly with radius, with $\tau_2 \approx 1$ Gyr in the inner disk and $\tau_2 = 7$ Gyr at the Solar annulus. This prescription was adopted to match the metallicity distribution of the Solar neighborhood and the bulge in the absence of mass-loaded outflows (Romano et al. 2000). We instead adopt an exponential $\tau_2 - R_{\rm gal}$ relation, with $\tau_2(R_\odot) = 15$ Gyr at the Solar annulus and a scale radius $R_{\tau_2} = 7$ kpc. This is similar to the star formation history timescale of Johnson et al. (2021), which was based on the stellar age gradients in Milky Way-like spirals observed by Sánchez (2020). We also run models with a linear prescription and with a uniform value for τ_2 and find little difference in our key results.

Finally, panel (c) of Figure 2 shows that the time of maximum infall $t_{\rm max}$ (c) strongly affects the overall stellar abundance distribution for values $t_{\rm max} \leq 2$ Gyr, but in this case the gas tracks do not produce the characteristic abundance loop. For $t_{\rm max} > 2$ Gyr, varying $t_{\rm max}$ results in a minor shift to the mean of the MDF and little change to the [O/Fe] distributions, even though the abundance tracks in [O/Fe]–[Fe/H] space appear very different. The value of $t_{\rm max}$ also slightly adjusts the ISM abundance endpoint, as a longer $t_{\rm max}$ means the chemical evolution "reset" from the second infall occurs closer to the present day (see discussion in Section 4.1. We adopt a fiducial value of $t_{\rm max} = 4.2$ Gyr, i.e. a lookback time of 9 Gyr, which is generally in line with previous two-infall studies (e.g., Nissen et al. 2020; Spitoni et al. 2020, 2021). This ensures that our models are compatible with the median age of the thick disk in the APOKASC-3 catalog of 9.14 ± 0.05 Gyr (Pinsonneault et al. 2025).

The Milky Way's last major merger with the dwarf galaxy dubbed Gaia Sausage-Enceladus (GSE; Belokurov et al. 2018; Helmi et al. 2018) has been proposed as an important influence on the transition from the thick disk to the thin disk, as in Spitoni et al. (2024). Our fiducial value of $t_{\rm max} = 4.2$ Gyr places the start of the formation of the thin disk close to the GSE merger (within uncertainties), which likely occurred ~ 10 Gyr ago (e.g., Helmi et al. 2018; Gallart et al. 2019; Naidu et al. 2021; Woody et al. 2025).

We note that all our models are normalized to produce the same thick-to-thin-disk mass ratio of $f_\Sigma(R_\odot) = 0.12$ (Bland-Hawthorn & Gerhard 2016) at the Solar annulus regardless of the infall parameters. The high-α sequence appears much less prominent in our [O/Fe] distributions in Figure 2 than in the data because the model outputs include only stars which were formed in-situ at the Solar annulus. In our multi-zone models, most of the high-α stars present in the Solar neighborhood have migrated from the inner Galaxy.

3.5. *The Star Formation Law*

The star formation law follows a single power-law prescription: $\dot{\Sigma}_\star \propto \Sigma_g^N$, with $N = 1.5$ following Kennicutt (1998). Previous work with this GCE model (e.g., Johnson et al. 2021; Dubay et al. 2024) assumed a three-

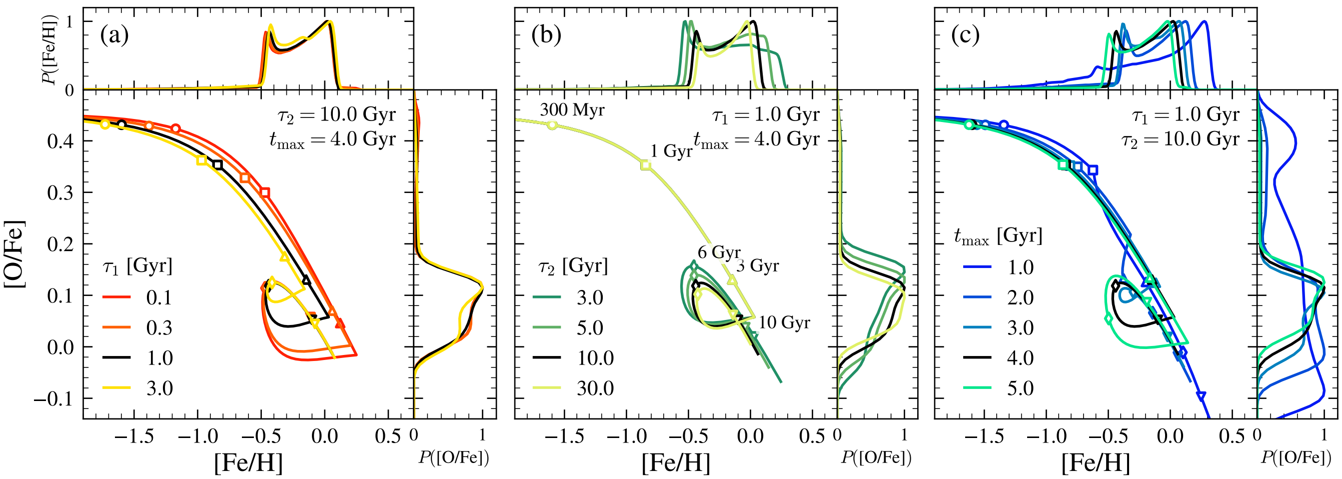

Figure 2. Gas abundance tracks in the [O/Fe]–[Fe/H] plane for one-zone chemical evolution models which assume different values for the infall history parameters. In each panel, one parameter is varied according to the legend while the other two are held fixed. The open symbols along each curve mark logarithmic steps in time, as denoted in panel (b). The marginal panels show the corresponding stellar abundance distributions, which are convolved with a Gaussian kernel with a width of 0.02 dex for visual clarity. All models use the $y/Z_\odot = 1$ yield set and assume $\eta = 0.2$.

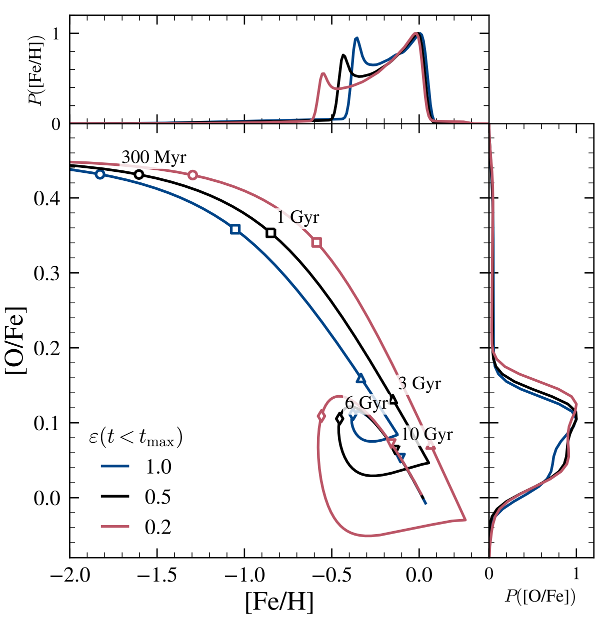

Figure 3. Effect of the SFE timescale pre-factor ε on abundance tracks and distributions in a one-zone model (see Section 3.5). All models are normalized to produce roughly the same ratio of thick to thin disk stars regardless of the value of ε during the first infall epoch.

component power-law, but we adopt a single power-law prescription in this work to allow for a more direct comparison with previous two-infall studies (e.g., Spitoni et al. 2024).

In detail, we calculate the star formation efficiency (SFE) timescale $\tau_\star \equiv \Sigma_g/\dot{\Sigma}_\star$ according to the following:

$$\tau_\star = \begin{cases} \varepsilon(t)\tau_{\rm mol}(t), & \Sigma_g \geq \Sigma_{g,0} \\ \varepsilon(t)\tau_{\rm mol}(t)\left(\frac{\Sigma_g}{\Sigma_{g,0}}\right)^{-1/2}, & \Sigma_g < \Sigma_{g,0} \end{cases} \tag{10}$$

where $\Sigma_{g,0} = 10^8\,{\rm M}_\odot\,{\rm kpc}^{-2}$ and $\tau_{\rm mol}(t) = \tau_{\rm mol,0}(t/t_0)^\gamma$, with $\gamma = 1/2$, $t_0 = 13.8\,$Gyr and $\tau_{\rm mol,0} = 2\,$Gyr Leroy et al. (2008). Previous two-infall studies (e.g., Nissen et al. 2020) have adopted a higher SFE during the first infall epoch than during the second, which we emulate through the pre-factor ε:

$$\varepsilon(t) = \begin{cases} 0.5, & t < t_{\rm max} \\ 1.0, & t \geq t_{\rm max}. \end{cases} \tag{11}$$

A lower value of $\varepsilon(t < t_{\rm max})$ leads to more efficient star formation during the first infall epoch. Figure 3 illustrates that this pre-factor largely affects the metallicity of the high-α sequence, with a smaller ε producing faster enrichment during the first infall and stronger dilution after $t_{\rm max}$. The pre-factor has virtually no effect on the overall [O/Fe] distribution because the model is normalized to produce the same thick-to-thin-disk mass ratio regardless of the details of the star formation law, but a lower value of ε does narrow the MDF by ~ 0.1 dex in [Fe/H]. We adopt $\varepsilon(t < t_{\rm max}) = 0.5$ for consistency with the two-infall literature. To guard against overcorrecting the SFE in the early Galaxy, we have tested eliminating either $\varepsilon(t)$ or $\tau_{\rm mol}(t)$ from our SFE prescription in multi-zone models and found no substantial difference to our results.

Figure 4 plots the star formation history of several different zones from our fiducial model with $y/Z_\odot = 1$.

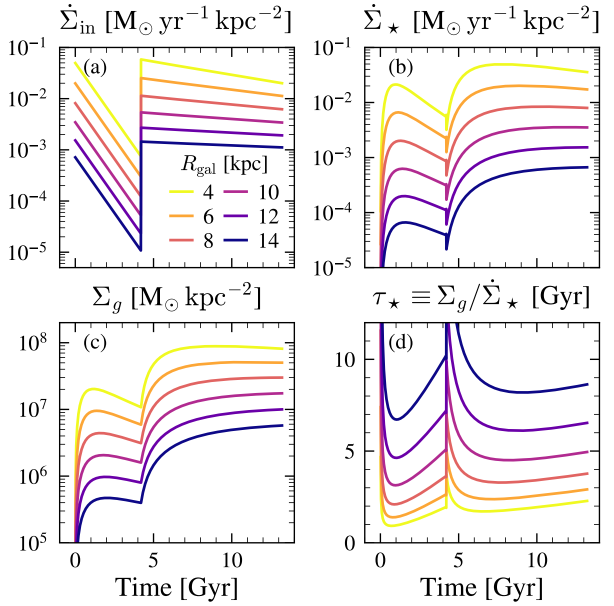

Figure 4. (a) The infall surface density, (b) the star formation surface density, (c) the gas surface density, and (d) the star formation efficiency timescale as a function of time for our fiducial multi-zone model with $y/Z_\odot = 1$. Each panel plots the history for six different zones of width $\delta R_{\rm gal} = 0.1$ kpc, color-coded by Galactocentric radius.

In the inner Galaxy, the infall rate $\dot{\Sigma}_{\rm in}$ is similar at the start of the first and second infall epochs, and the star formation rate peaks at $t \approx 7$ Gyr. In the outer Galaxy, the infall rate at $t_{\rm max}$ is significantly higher than at $t = 0$, and the star formation rate is highest at the present day. The star formation efficiency timescale $\tau_\star$ spikes near $t = 0$ and $t_{\rm max}$, but otherwise increases throughout the model's duration, reaching a maximum of $\tau_\star \approx 2$ Gyr in the inner disk and $\tau_\star \approx 9$ Gyr in the outer disk.

3.6. *Stellar Migration*

This study is not the first to apply a prescription for radial migration to a two-infall GCE model. Spitoni et al. (2015) explored the effect of migration speeds of order $\sim 1\,{\rm km s}^{-1}$ on the metallicity distribution of the Solar neighborhood. They prescribed some fraction of stars from the inner and outer Galaxy which contribute to the local present-day population based on a constant migration speed, and they also assumed some fraction of stars born in the Solar neighborhood will have migrated elsewhere. This method can improve agreement with the observed local metallicity distribution, but does not scale to abundance distributions across the disk. Palla et al. (2022) compared the Spitoni et al. (2015) prescription to the diffusion treatment of Frankel et al. (2018) and found similar results. Our implementation, described below, affects abundance distributions across the Galaxy, not just at the Solar annulus.

The distance a stellar population born at $R_{\rm form}$ migrates over its age τ is drawn from a Gaussian centered at 0 with standard deviation

$$\sigma_{\rm RM} = \sigma_{\rm RM8}\left(\frac{\tau}{8\,{\rm Gyr}}\right)^{0.33}\left(\frac{R_{\rm form}}{8\,{\rm kpc}}\right)^{0.61}, \tag{12}$$

where we adopt $\sigma_{\rm RM8} = 2.68$ kpc as the fiducial value for the strength of radial migration. This is smaller than the value of $\sigma_{\rm RM8} = 3.6$ kpc found by Frankel et al. (2018), but in Section 4.1 we explore the effect of a stronger migration prescription.

All stellar populations are born at the Galactic midplane and are assigned a final midplane distance z drawn from the distribution

$$p(z|\tau, R_{\rm final}) = \frac{1}{4h_z}{\rm sech}^2\left(\frac{z}{2h_z}\right), \tag{13}$$

where $R_{\rm final}$ is the final Galactocentric radius of the stellar population. The width of the distribution h_z is given by

$$h_z(\tau, R_{\rm final}) = \left(\frac{0.24\,{\rm kpc}}{e^2}\right)\exp\left(\frac{\tau}{7\,{\rm Gyr}} + \frac{R_{\rm final}}{6\,{\rm kpc}}\right). \tag{14}$$

We note that the final midplane distance is assigned at the end of the model run and therefore does not affect the chemical evolution.

The parameters of Equations 12 and 14 were chosen to fit the stellar migration patterns in the `h277` hydrodynamical simulation (Christensen et al. 2012). A more complete discussion of the migration scheme and its consequences can be found in Appendix C of Dubay et al. (2024).

We note an important distinction between our method and that of Spitoni et al. (2015): SNe Ia from long-lived progenitors contribute Fe to each zone they migrate through, not just their birth zone. This is important because the median delay time of our SN Ia DTD is ~ 2 Gyr, for which the width of the migration distribution is $\sigma_{\rm RM} \approx 2$ kpc (Equation 12). So, a significant fraction of SN Ia progenitors born in a given zone will enrich a disparate region of the Galaxy.

4. MULTI-ZONE MODEL RESULTS

4.1. *Dilution & Approach to Equilibrium*

The dilution effect discussed in Section 3.1 is clearly seen in the multi-zone model results. We first examine the differences between multi-zone models which assume different yield and outflow scales. Figure 5 shows stellar age–abundance relations produced by models with $y/Z_\odot = 1$ and $y/Z_\odot = 2$ with fiducial parameters (Table 3). The $y/Z_\odot = 1$ model (column a) shows two

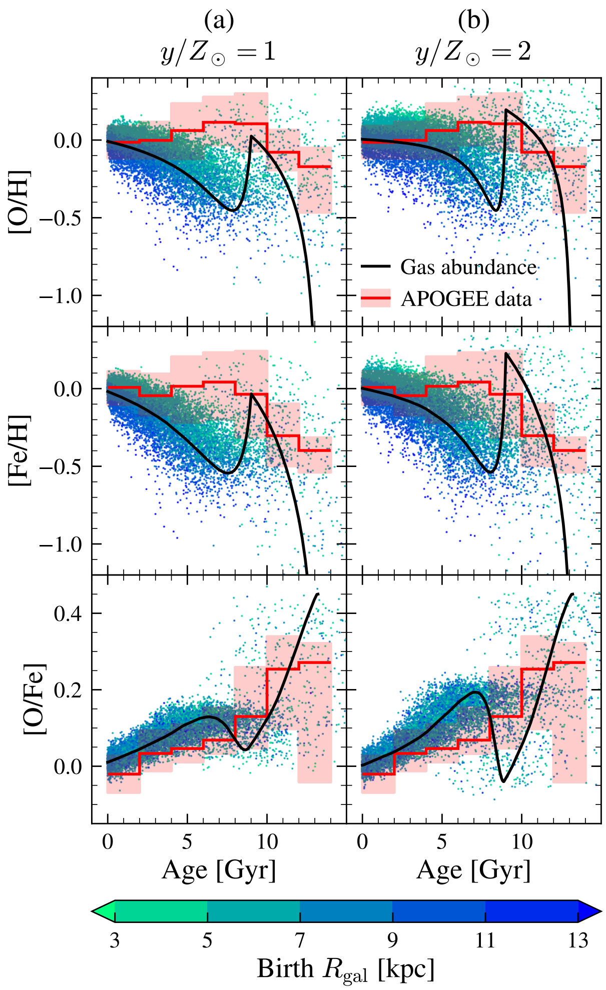

Figure 5. Stellar age–abundance relations predicted by multi-zone models which assume the fiducial parameters with different yield sets and outflow mass-loading factors. Each point represents a stellar population drawn from the Solar neighborhood near the midplane ($7 \leq R_{\rm gal} \leq 9$ kpc, $0 \leq |z| \leq 0.5$ kpc) and is color-coded by its birth radius. A Gaussian scatter is applied to each point according to the median age and abundance uncertainties in Table 2. For visual clarity, we plot only a random mass-weighted sample of 10 000 points in each panel. The black curve plots the ISM abundance at $R_{\rm gal} = 8$ kpc over time. The red line segments plot the median abundance for APOGEE stars in 2 Gyr-wide age bins, and the shaded regions represent the 16th–84th percentiles in each bin. Age estimates for APOGEE stars come from Leung et al. (2023). **Key takeaway:** Both models feature a major dilution event at a lookback time of 9 Gyr, and for model (a) the dilution persists throughout much of the thin disk epoch.

clear discrepancies with the Leung et al. (2023) age–abundance relation: a major ~ 0.5 dex dilution at a lookback time of ~ 9 Gyr near where the data show a maximum in [O/H], and non-zero abundance evolution at late times where the data show very little abundance evolution. The evolution of [Fe/H] is similar, but the approach to the final metallicity is slower because of the additional delay imposed on Fe production from SNe Ia. The $y/Z_\odot = 2$ yield set (column b) mitigates both of these issues by shortening the time it takes the ISM metallicity to rebound post-$t_{\rm max}$, producing a much flatter abundance curve at late times. However, model (b) produces a poorer fit to the age–[O/Fe] relation: the decline in [O/Fe] over the thin disk epoch is steeper than the data, especially for ages $\sim 4 - 8$ Gyr.

We next attempt to mitigate the dilution and late-time evolution problems for the empirical ($y/Z_\odot = 1$) yield scale. Figure 6 shows the effect of varying several parameters for the $y/Z_\odot = 1$ model: (b) the strength of radial migration $\sigma_{\rm RM8}$, (c) the metallicity of the infalling gas $[{\rm X/H}]_{\rm CGM}$, and (d) the local thick-to-thin disk density ratio $f_\Sigma(R_\odot)$.

The observed rise in the median metallicity of stars with ages of $\sim 4 - 10$ Gyr could be due to radial migration, as those stars were probably not born in-situ, but rather migrated from the dense inner metal-rich regions of the Galaxy (Feuillet et al. 2018). Although our fiducial model does include a prescription for radial migration, the majority of stars in that age range in Figure 5 still have sub-Solar abundances. Therefore, column (b) of Figure 6 presents a model with $y/Z_\odot = 1$ and a stronger migration prescription of $\sigma_{\rm RM8} = 5$ kpc. As a result, the stars which make up the present-day Solar neighborhood are drawn from a wider range of birth $R_{\rm gal}$, producing a broader abundance distribution for any given age. However, even though this prescription is much stronger than the estimates of, e.g., Frankel et al. (2018), the model still significantly under-predicts the metallicity of $\sim 4 - 9$ Gyr old stars.

Next, we investigate a model where the infalling gas is enriched to a metallicity $[{\rm O/H}] = [{\rm Fe/H}] = [{\rm X/H}]_{\rm CGM}$ before accreting onto the disk. Column (c) of Figure 6 shows results for the case where $[{\rm X/H}]_{\rm CGM} = -0.5$, the highest metallicity allowed by the local low-α population. Pre-enriched infall at this level mitigates but does not completely solve the two discrepancies. The dilution effect of the second infall is reduced to the ~ 0.3-dex level as the gas which replenishes the Galaxy's reservoir is no longer pristine; however, the width of the stellar abundance distribution at any given age is also reduced, because the enriched gas accretion imposes a lower limit on the metallicity of the outermost regions, from which

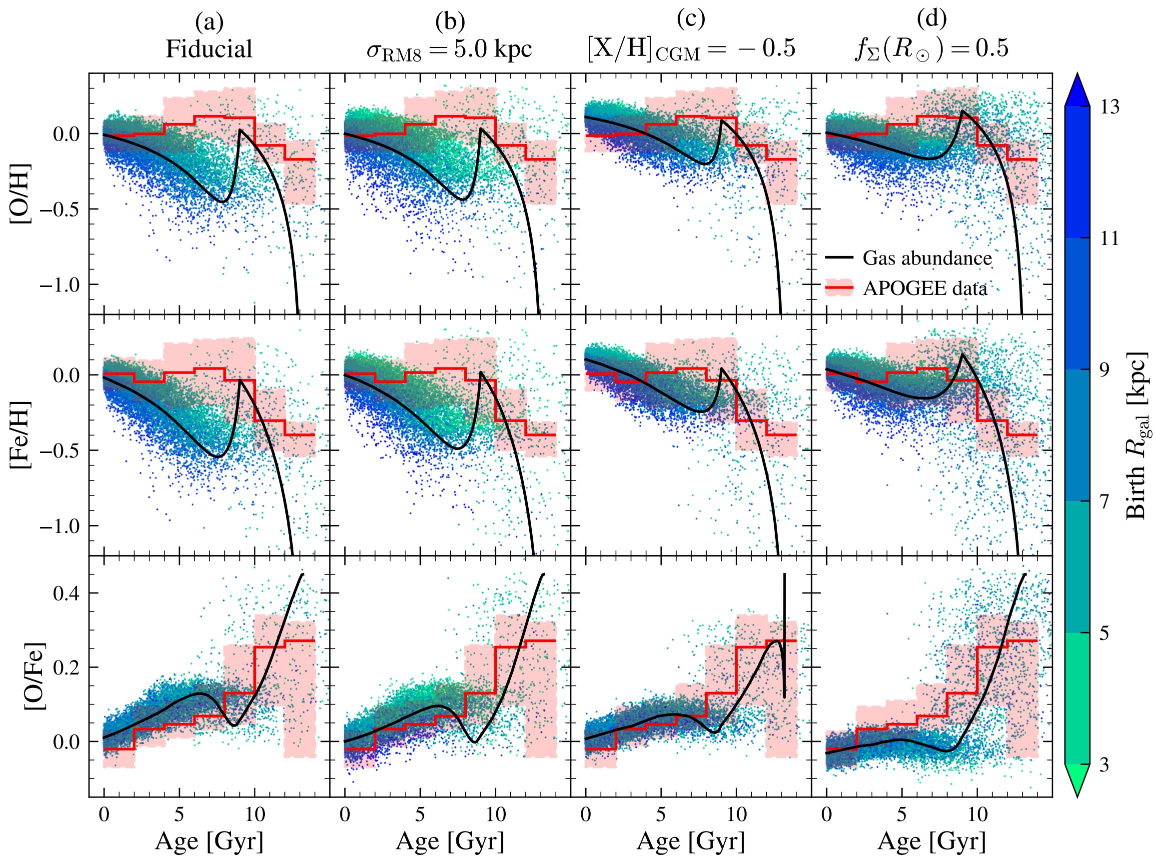

Figure 6. Stellar age–abundance relations in the Solar annulus produced by select multi-zone models with $y/Z_\odot = 1$. The layout is similar to Figure 5. Each column shows results from a different multi-zone model: **(a)** our fiducial model with $y/Z_\odot = 1$, $\sigma_{\rm RM8} = 2.7\,{\rm kpc}$, pristine gas infall, and $f_\Sigma(R_\odot) = 0.12$; **(b)** a model with greater radial migration strength $\sigma_{\rm RM8} = 5\,{\rm kpc}$; **(c)** a model that assumes the infalling gas has metallicity $[{\rm O/H}]_{\rm CGM} = [{\rm Fe/H}]_{\rm CGM} = -0.5$; and **(d)** a model with a higher local thick-to-thin disk ratio, $f_\Sigma(R_\odot) = 0.5$. **Key takeaway:** Model (d) comes the closest to the observed age–metallicity relation at the expense of the age–[O/Fe] relation, but no model completely reconciles the dilution problem.

the stars of the low-metallicity tail in the Solar neighborhood are drawn. The late-time gas abundance evolution is similar to the fiducial model, but it ends at slightly super-Solar metallicity—an effect which can be compensated by a slightly increased value of η. This model also narrows the [O/Fe] distribution of mono-age populations (almost all the model stars fall within the 1σ band of the data), which could be compensated for by stronger radial migration.

Finally, we explore a model where the local thick-to-thin disk surface density ratio is ~ 4 times larger that the fiducial value, $f_\Sigma(R_\odot) = 0.5$. This is higher than most of the constraints from population counts or GCE models (see Section 3.3). Column (d) of Figure 6 shows that requiring a more massive thick disk can reduce the dilution and recent evolution of the ISM, similar to the pre-enriched infall, because more of the gas disk is built up during the first infall phase. The model produces the best agreement with the observed age–[Fe/H] relation (second row). However, agreement with the observed age–[O/Fe] relation is poor, with the model predicting less evolution in [O/Fe] over the past ~ 9 Gyr than observed by ≈ 0.1 dex.

Overall, no modification to the $y/Z_\odot = 1$ model is able to completely overcome both the dilution and late-time evolution issues. Pre-enrichment of the accreted gas and a higher disk mass ratio can reduce the discrepancy with the data, but they cause issues of their own in the age–[O/Fe] plane.

4.2. *Abundance Evolution Across the Disk*

The discrepancies between the predicted and observed abundance evolution in the Solar neighborhood discussed in Section 4.1 persist across the Galactic disk. Figure 7 shows the evolution of the MDF with age across five radial bins for the $y/Z_\odot = 1$ and $y/Z_\odot = 2$ models with the fiducial parameters. For the APOGEE sample, we use the [C/N]-derived age estimates due to the larger

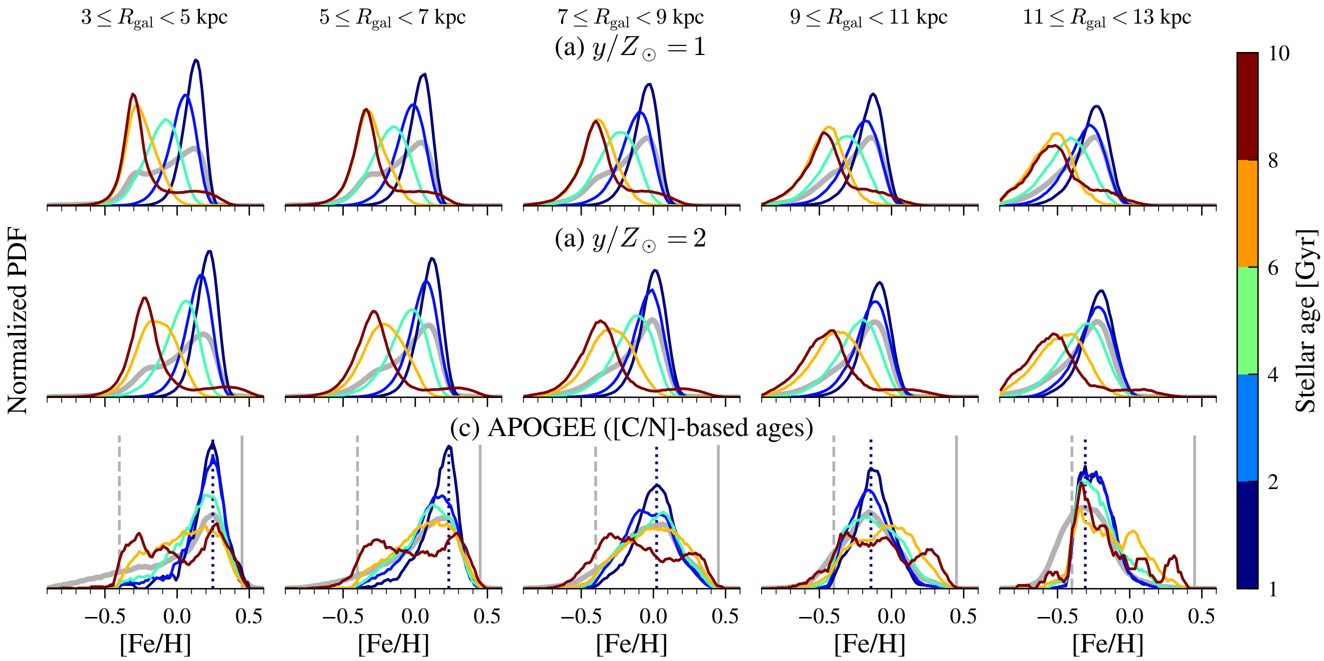

Figure 7. Evolution of the MDF over time across the Galactic disk. In each panel, normalized stellar [Fe/H] distributions within a 2 kpc-wide annulus are color-coded by the stellar age range. The gray curve represents the total MDF in each region. Rows (a) and (b) present the distributions from multi-zone GCE models with the fiducial parameters (see Table 3) at different yield and outflow scales. A Gaussian scatter has been applied to each model stellar population in rows (a) and (b) according to the median [C/N]-derived age and abundance uncertainties in Table 2. Row (c) presents the distributions from APOGEE DR17 with ages derived from [C/N] abundances (see Section 2). The vertical blue dotted lines in row (c) mark the mode of the distribution in the $1-2$ kpc age bin for reference. Also in row (c), the gray dashed line marks the cut at $[\mathrm{Fe/H}] > -0.4$ for upper red giant branch and red clump stars, and the gray solid line marks the cut at $[\mathrm{Fe/H}] < +0.45$ for all stars with [C/N]-based ages. The distributions in all panels are restricted to $0 \leq |z| < 0.5$ kpc and boxcar-smoothed with a width of 0.1 dex for visual clarity. **Key takeaway:** The APOGEE distributions show remarkably little variation in position over the past $\sim 6-8$ Gyr at all radii, whereas both GCE models predict a steady evolution toward higher [Fe/H] with time.

sample size in the most distant regions of the disk; we limit the comparison to ages in the range $1-10$ Gyr because of large systematic uncertainties for the oldest stars, as discussed in Section 2.

The results of both models in Figure 7 show a clear evolutionary trend at all radii. The mode of the MDF shifts consistently to the right when moving from older to younger stars. The distance between the $1-2$ Gyr and $2-4$ Gyr age bins is smaller for the $y/Z_\odot = 2$ model because of the faster approach to equilibrium (see also Figure 5). In the Solar annulus (center column), the mode of the $6-8$ Gyr age MDF is 0.3 dex lower than the present-day metallicity in the $y/Z_\odot = 2$ model, and 0.4 dex lower in the $y/Z_\odot = 1$ model.

In contrast, the APOGEE data show remarkably little evolution over the past ~ 8 Gyr at all radii. Row (c) of Figure 7 shows that the MDF broadens with age, but its peak does not shift much over the past ~ 8 Gyr. The mode [Fe/H] for the youngest stars (indicated by the vertical blue dotted line) is nearly the same as for the $6-8$ Gyr old stars. Inward of the Solar annulus, the MDF skews more to lower [Fe/H], but its mode does not shift by more than ~ 0.1 dex. It is difficult to draw conclusions about the outer Galaxy because the mode [Fe/H] is close to the metallicity cut at $[\mathrm{Fe/H}] > -0.4$ for luminous giants (represented by the vertical gray dashed line), which comprise the majority of stars in the sample at that distance. The remarkable consistency of the MDF over time, in agreement with the equilibrium scenario of Johnson et al. (2024), contrasts with the predictions of our fiducial models.

The oldest age bin in Figure 7 shows distinct behavior in both the models and data. The $8-10$ Gyr age bin spans both the tail end of the thick disk phase and the beginning of the thin disk, so the MDF is bimodal: the higher peak consists of > 9 Gyr old stars, and the lower peak $8-9$ Gyr old stars (post-dilution phase). Intriguingly, the APOGEE MDF in that age bin is also bimodal in all but the outer-most radial bin, with peaks at $[\mathrm{Fe/H}] \approx -0.3$ and $+0.3$ independent of the location in the Galaxy. While data and model show qualitatively similar behavior, they actually represent different populations. In the model, the metal-rich peak is composed of thick-disk stars while the metal-poor peak marks the formation of the thin disk. In the data, the metal-rich peak are all low-α stars, while the metal-poor peak is the locus of the high-α sequence —a reversal of the model predictions.

4.3. *The Local Abundance Topology*

The two-infall model explains the chemical evolution of the thin disk through the low-α loop (see discussion in Section 3.4). However, inspection of the marginal [O/Fe] distributions in, e.g., Figure 1 reveals a different morphology of the low-α sequence: the two-infall model predicts two peaks in [O/Fe] in the thin disk where the data show only one. The location of the second peak, at intermediate [O/Fe], varies depending on the yields (Figure 1) and infall parameters (Figure 2), but is always present. This morphology remains essentially consistent in our multi-zone models as well, despite the inclusion of radial mixing and vertical dispersion of stars.

Figure 8 illustrates the origin of the intermediate-α peak predicted by the two-infall model at mid to high Galactic latitudes. Between $0.5 \leq |z| < 1$ kpc, both the models with $y/Z_\odot = 1$ and $y/Z_\odot = 2$ predict an over-density of stars near the abundance turn-over ([Fe/H] ≈ -0.3, [O/Fe] $\approx 0.1 - 0.2$), which is not seen in the APOGEE sample. This over-density occurs because the overall rate of chemical evolution slows down ~ 2 Gyr after the second infall, and at the same time the delayed enrichment from SNe Ia reverses the evolution of [O/Fe]. This is a generic prediction of *any* two-infall model regardless of its specific parameters, though its impact can be mitigated through parameter choices which act to compress the distance between the low- and intermediate-α peaks, as in the $y/Z_\odot = 1$ model in Figure 1 or the models with longer τ_2 in Figure 2.

Additionally, the shape of the low-α sequence in the model results (a concave-down "comma") is clearly different from the data (a concave-up "swoosh"). This problem is not unique to the two-infall scenario: it results from the concave-down track of the abundance evolution, and has stymied other models as well (e.g., Minchev et al. 2013; Johnson et al. 2021; Prantzos et al. 2023). Nevertheless, it is worth mentioning because the two-infall scenario is otherwise quite successful at reproducing the local stellar distribution in [O/Fe]–[Fe/H] space.

4.4. *Global Abundance Distributions*

4.4.1. *The [O/Fe] Distribution: Two or Three Peaks?*

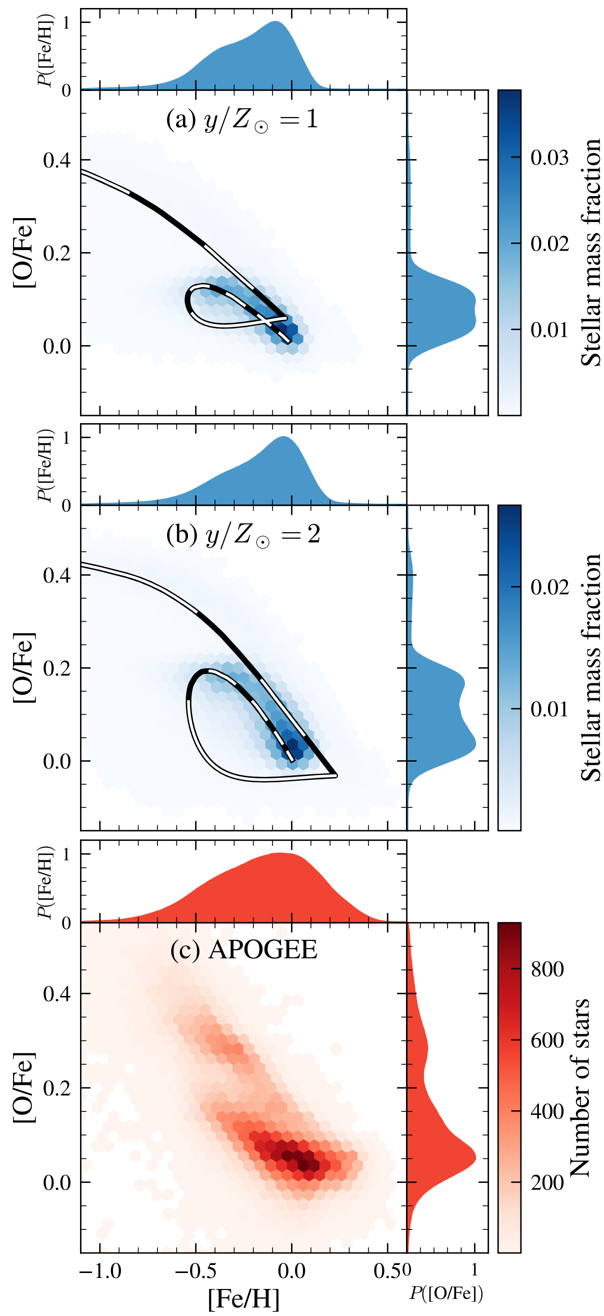

Figure 8. The density of stars in the [O/Fe]–[Fe/H] plane predicted by multi-zone models with (a) $y/Z_\odot = 1$ and (b) $y/Z_\odot = 2$, and (c) from the APOGEE DR17 catalog. The curves in panels (a) and (b) plot the ISM abundance at the Solar annulus over time, and the alternating black and white segments mark time intervals of 1 Gyr. The model output has been re-sampled to match the APOGEE stellar $|z|$ distribution, and a Gaussian scatter has been applied to the predicted abundances according to Table 2. Stars in all panels are restricted to the region defined by $7 \leq R_{\rm gal} < 9$ kpc and $0 \leq |z| < 2$ kpc. **Key takeaway:** the two-infall model generically predicts a stellar over-density at intermediate [O/Fe] and low metallicity, which is not observed in APOGEE.

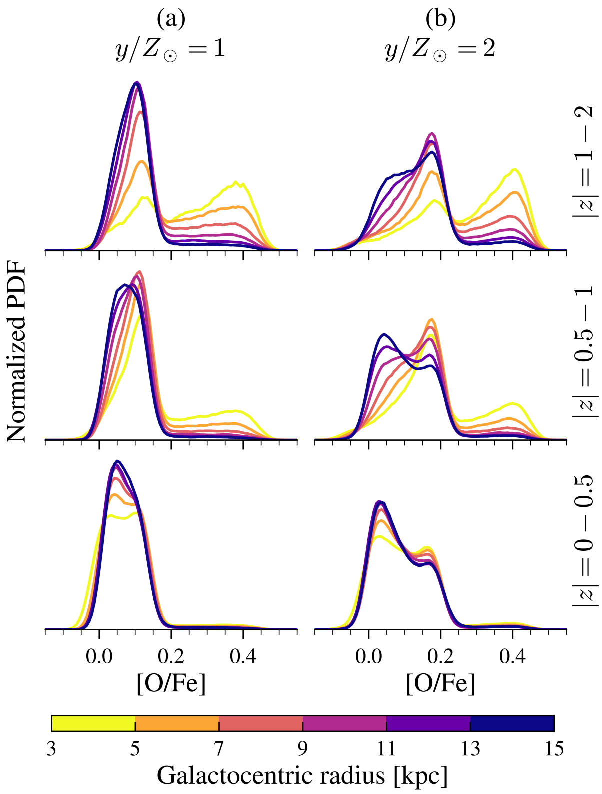

Figure 9. Normalized stellar [O/Fe] distributions produced by multi-zone models which assume the fiducial parameters with different yield sets and outflow mass-loading factors. Each row presents stellar distributions within a range of absolute midplane distance $|z|$ reported on the far right, and the vertical scale is consistent across each row. Within each panel, the distributions are color-coded according to the bin in galactocentric radius $R_{\rm gal}$ from which they are drawn. The median APOGEE abundance uncertainties are forward-modeled onto the model outputs (see Table 2). For visual clarity, each distribution is smoothed with a box-car of width 0.05 dex. **Key takeaway:** The two-infall model produces an intermediate-[O/Fe] peak that is especially prominent in the $y/Z_\odot = 2$ model at mid to high latitudes.

The two-infall model generically predicts *three* peaks in the [O/Fe] distribution, which correspond to the high-α sequence, the abundance "turn-over" after the second infall, and finally the late-time low-α sequence. We previously noted this feature in Dubay et al. (2024). Figure 9 compares [O/Fe] distributions from across the Galactic disk produced by models with the $y/Z_\odot = 1$ and $y/Z_\odot = 2$ yield sets. We present the distributions in multiple bins of $|z|$ as well as $R_{\rm gal}$ because the observed pattern varies as a function of midplane distance, and because the APOGEE selection function over-emphasizes high-$|z|$, and therefore high-α, stars in the full sample. For model (a) with $y/Z_\odot = 1$, the two thin disk peaks are close enough together that they approximate a single peak, especially once observational uncertainties are factored in. With the $y/Z_\odot = 2$ yield set, however, there is a ~ 0.2 dex separation between the low- and intermediate-α peaks thanks to increased efficiency of CCSN element production. As a result, model (b) predicts a high density of stars at [O/Fe] $\approx +0.2$ where the data show a relatively low density.

In Figure 10, we show the result of our attempts to mitigate the intermediate-α peak discrepancy for the $y/Z_\odot = 2$ yield set in a few different ways, namely by reducing the size of the thin disk loop seen in panel (b) of Figure 8. First, we substitute our fiducial SN Ia DTD with a simple power-law,

$$f_{\rm Ia}^{\rm plaw}(t) = (t/1\,{\rm Gyr})^{-1.1}, \qquad (15)$$

which reduces the median SN Ia delay time from ~ 2 Gyr to ~ 0.5 Gyr. As shown in column (b), this has the intended effect on the low-α sequence, but it also entirely eliminates the high-α peak. Dubay et al. (2024) discuss in detail why such a DTD is disfavored by Milky Way stellar abundances, and their results hold true for the two-infall model as well.

Next, in model (c) the metallicity of the infalling gas increases to $[{\rm X/H}]_{\rm CGM} = -0.5$ at late times. We choose this value because if it were any higher, the infalling gas would have higher metallicity than the most metal-poor thin disk stars. This model results in very similar [O/Fe] distributions to the $y/Z_\odot = 1$ case. We assume that the infalling gas has [O/Fe] = 0 at all times; an alternate run with [O/Fe] = +0.3 shifted the distribution towards higher [O/Fe], worsening agreement with observations.

Finally, in model (d) we increase the local thick-to-thin disk surface density ratio by a factor of 4 to $f_\Sigma(R_\odot) = 0.5$. This value means that 1 in 3 stars in the Solar annulus belong to the thick disk and is on the high end of estimates (see Section 3.3). The result as shown in Figure 10 is a true bimodal abundance distribution, with a more prominent high-α peak than in the previous models. In summary, either pre-enriched infall or an enhanced disk mass ratio can improve agreement with the observed thin disk abundances for the $y/Z_\odot = 2$ case. These parameters also help the model better fit the age–metallicity relation, as shown in Section 4.1 for the $y/Z_\odot = 1$ case.

4.4.2. *The Best Model*

Motivated by the results of the previous sections, we construct a model which attempts to solve all of the issues that have been outlined thus far. Our "best attempt" model uses the $y/Z_\odot = 2$ yield set to flatten the local age–metallicity relation (Figure 5), pre-enriched

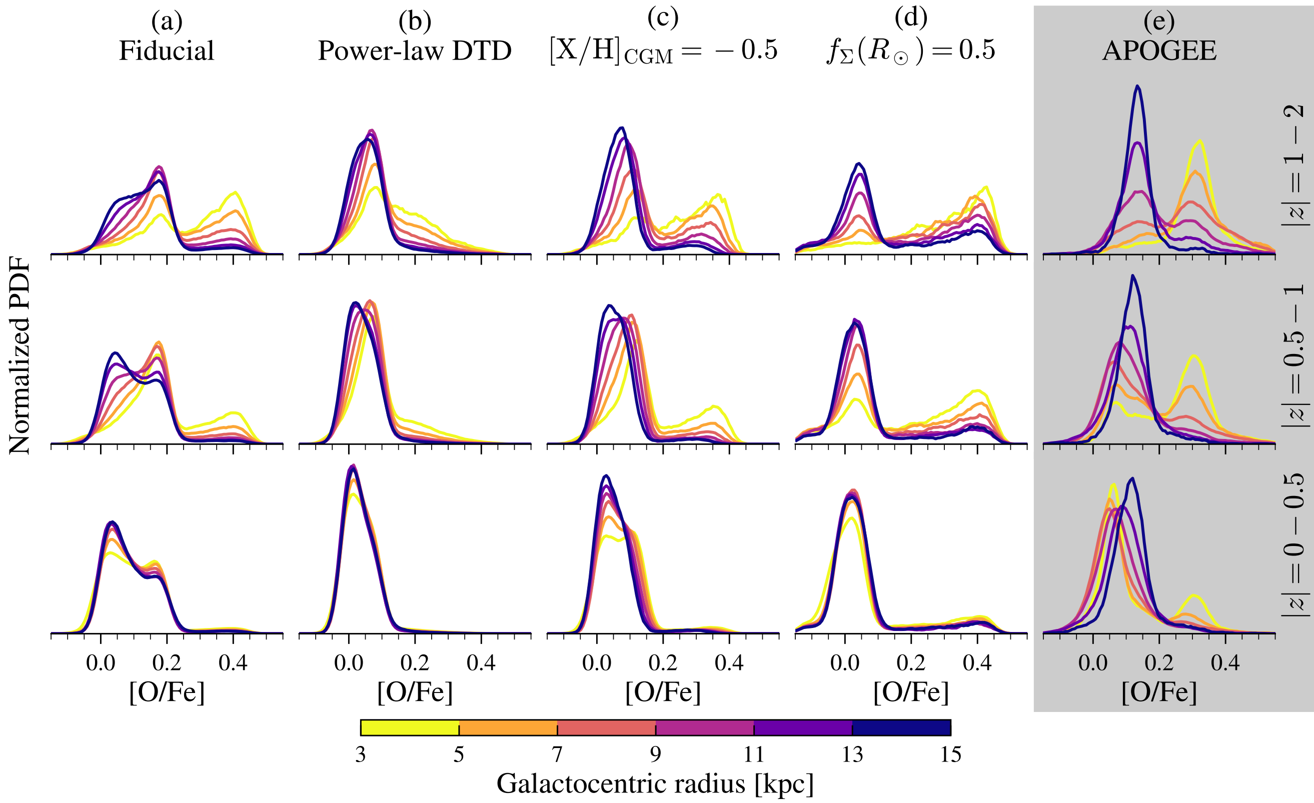

Figure 10. Stellar [O/Fe] distributions produced by select multi-zone models with $y/Z_\odot = 2$ (a–d) and as observed by APOGEE (e). The layout is similar to Figure 9. Each column shows results from a different multi-zone model: **(a)** the fiducial model with $y/Z_\odot = 2$, the fiducial DTD, pristine gas infall, and $f_\Sigma(R_\odot) = 0.12$ (identical to column (b) of Figure 5); **(b)** a model that adopts a power-law DTD; **(c)** a model that assumes the infalling gas has metallicity $[\mathrm{O/H}]_{\mathrm{CGM}} = [\mathrm{Fe/H}]_{\mathrm{CGM}} = -0.5$; and **(d)** a model with a higher local thick-to-thin disk ratio, $f_\Sigma(R_\odot) = 0.5$. **Key takeaway:** For the $y/Z_\odot = 2$ case, pre-enrichment of the accreted gas or a higher thick-to-thin disk ratio can improve the low-α distribution while preserving the high-α peak.

infall at the level of $[\mathrm{X/H}]_{\mathrm{CGM}} = -0.7$ to reduce the dilution at $t_{\max}$ (Figure 6), slightly stronger outflows with $\eta_\odot = 1.8$ to maintain the local equilibrium at Solar metallicity, moderately stronger radial migration with $\sigma_{\mathrm{RM8}} = 3.6$ kpc to widen the local metallicity dispersion (Figure 6), and a greater local disk ratio $f_\Sigma(R_\odot) = 0.25$ to reduce the width of the low-α distribution and beef up the high-α sequence (Figure 10). Our choices for $[\mathrm{X/H}]_{\mathrm{CGM}}$, σ_{RM8}, and $f_\Sigma(R_\odot)$ are more moderate, and we believe more realistic, than in previous sections to avoid extreme effects resulting from the combination of these parameters. We stress that our focus is on qualitative rather than quantitative agreement with the data, and thus we do not attempt to find the optimal set of parameters through methods such as MCMC.

Figure 11 presents the stellar [O/Fe]–[Fe/H]–age distributions as a function of R_{gal} and $|z|$ predicted by the best multi-zone model. The model is generally successful at reproducing the observed distribution of stars in the [O/Fe]–[Fe/H] plane, especially in the inner Galaxy and close to the midplane (panels along the left and bottom sides of the figure, respectively). However, the predicted high-α sequence is less concentrated than in the data, and its presence is still significant even in the outer Galaxy—likely a consequence of the stronger migration prescription and higher thick-to-thin disk ratio. In general, the predicted distributions do not align with the data quite as well at large midplane distances ($1 \leq |z| < 2$ kpc), but this may partly be due to our prescription for vertical heating (see Section 3.6).

The model makes two notable predictions about the age–abundance distributions. First, there is a population of $\sim 8-9$ Gyr old stars at sub-Solar [O/Fe], especially at $|z| \geq 0.5$ kpc, formed immediately after the second infall during a period of rapid chemical evolution. These stars form a small percentage of the overall distribution (see also Figure 11 from Spitoni et al. 2024) but in this case they occupy a unique portion of the abundance space. A longer τ_1 could shift this population to higher [O/Fe] where it would be obscured by the rest

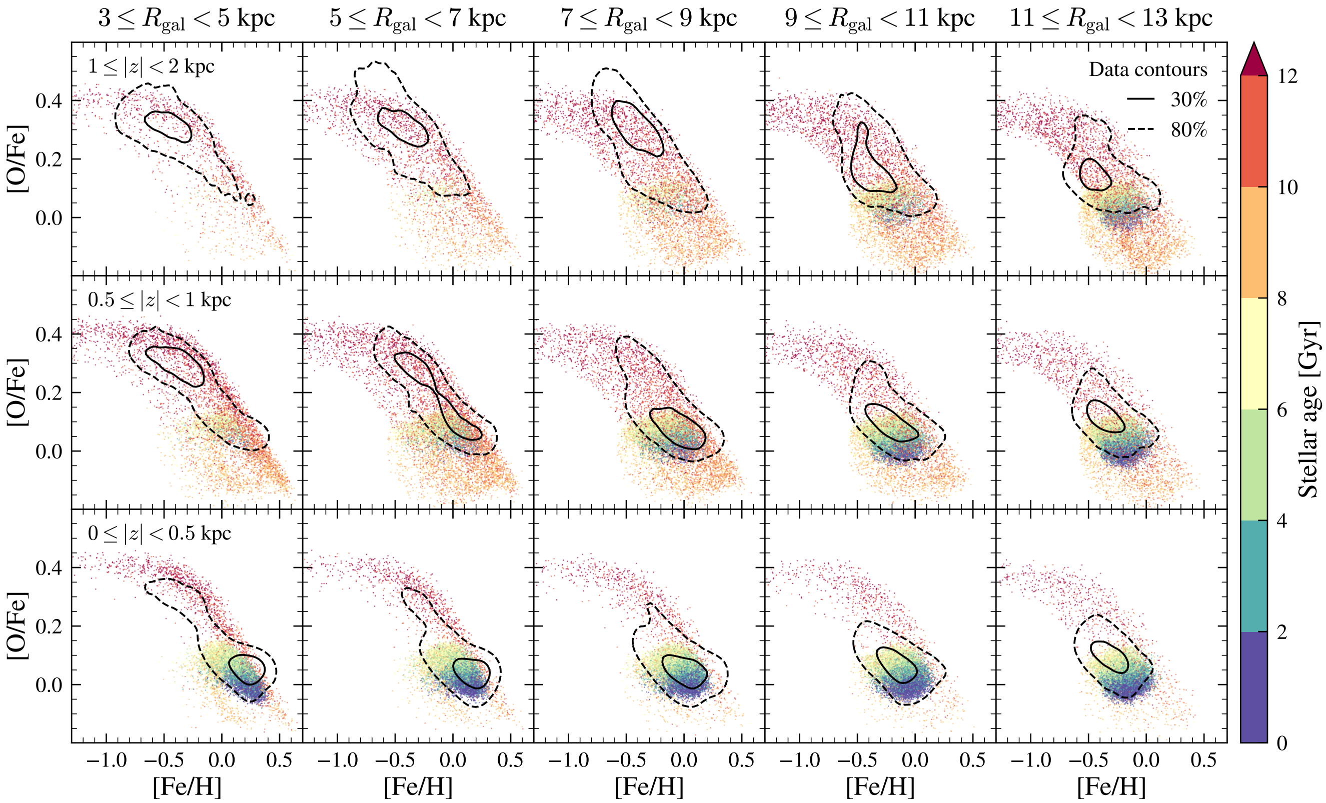

Figure 11. Stellar abundance distributions across the disk predicted by our best multi-zone model, with $y/Z_\odot = 2$, $[\mathrm{X/H}]_{\mathrm{CGM}} = -0.7$, $f_\Sigma(R_\odot) = 0.25$, $\sigma_{\mathrm{RM8}} = 3.6\,\mathrm{kpc}$, and $\eta_\odot = 1.8$. Each panel presents a random mass-weighted sample of 10 000 stellar populations that are drawn from the given (R_{gal}, $|z|$) bin and color-coded by age. A Gaussian scatter is applied to each point according to the median age ($\tau_{[\mathrm{C/N}]}$) and abundance uncertainties in Table 2. The solid and dashed contours enclose 30% and 80%, respectively, of the APOGEE data in each region. **Key takeaway:** The predicted distribution from the two-infall model lines up with the APOGEE distribution close to the midplane, but agreement is worse at higher latitudes and in the outer Galaxy.

of the low-α sequence (see Figure 2). Second, the stars born at the tail end of the thick and thin disk epochs are adjacent to each other in abundance space, meaning the two-infall model predicts a steep age gradient for the most metal-rich stars in a given region.

4.5. *Local Age Patterns*

The two-infall model makes a prediction about the local stellar age distribution that is fundamental to its construction: that the most metal-rich stars born in-situ in any region of the Galaxy come from the metal-rich tail of the first infall sequence, and are therefore older than all of the thin disk stars. As noted in the previous Section, this prediction is apparent in any of the panels in Figure 11, especially where $|z| < 0.5\,\mathrm{kpc}$. We investigate this prediction further here.

The top row of Figure 12 presents the median stellar age as a function of [O/Fe] and [Fe/H] for two multi-zone models and APOGEE. While the models predict a fairly accurate distribution of stars in abundance space, especially for the low-α population, the stellar age patterns are obviously quite different. In both the $y/Z_\odot = 1$ and $y/Z_\odot = 2$ models, there is a sharp divide in the median stellar age when moving from the thick disk ($\tau \geq 9\,\mathrm{Gyr}$) to the thin disk ($\tau \lesssim 5\,\mathrm{Gyr}$). The $y/Z_\odot = 2$ model also predicts that the stars with the lowest [O/Fe] should be $\sim 8-9\,\mathrm{Gyr}$ old, while these are some of the youngest stars in APOGEE. The latter issue can be mitigated by adjusting the parameters of the first infall, as discussed in the previous Section, but the former is not solved so easily.

We further highlight the discrepant age patterns in the bottom panels of Figure 12, which compare the overall stellar age distribution against that of the locally metal rich (LMR) stars, defined here as $[\mathrm{Fe/H}] \geq +0.1$.[1] For APOGEE, the distributions are similar, both peaking

[1] The precise location of the cut matters little, as we observe the same behavior for cuts ranging from +0.05 to +0.2 dex.

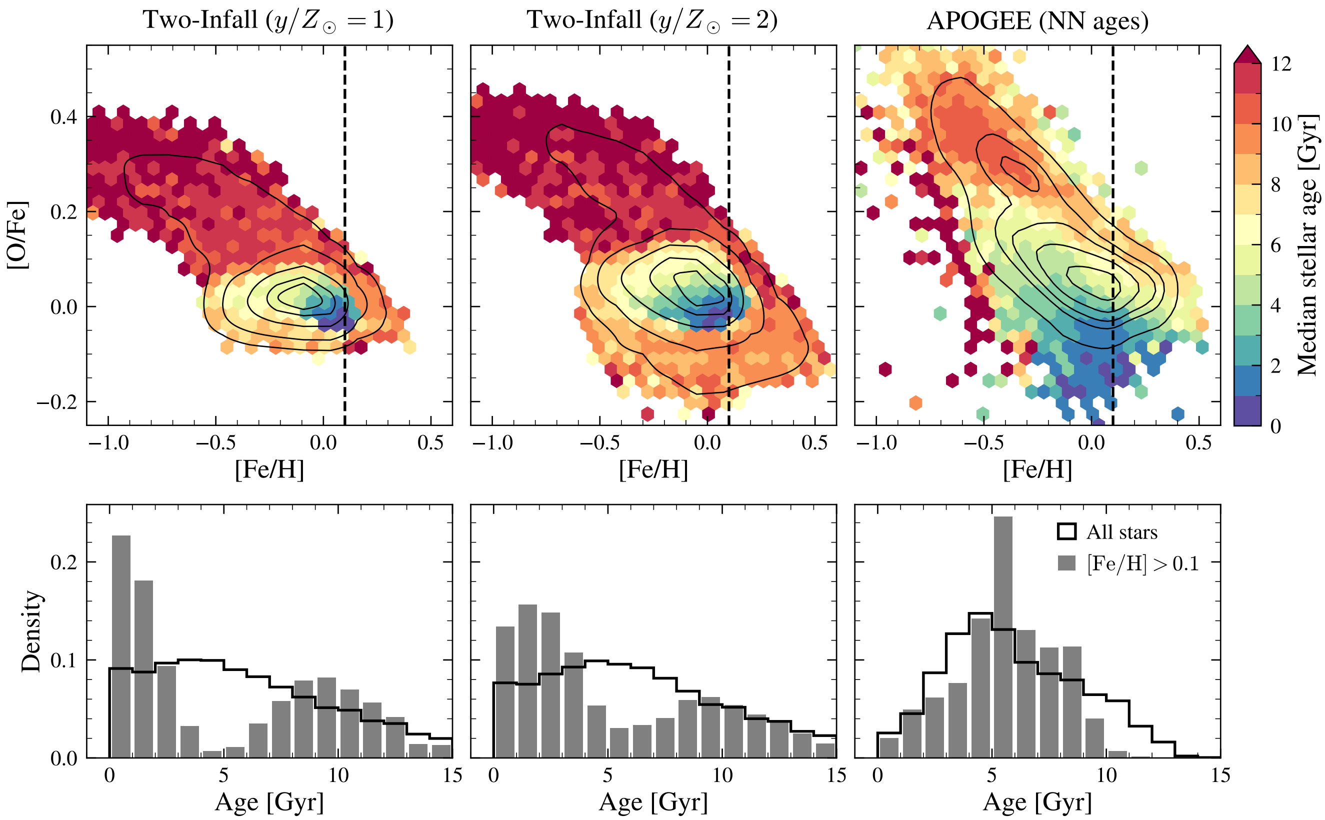

Figure 12. *Top:* The median stellar age as a function of [O/Fe] and [Fe/H] in the Solar annulus ($7 \leq R_{\rm gal} < 9\,$kpc, $0 \leq |z| < 2\,$kpc). The left and center panels plot the output of our best two-infall models, with $y/Z_\odot = 2$, $[\rm X/H]_{\rm CGM} = -0.7$, $f_\Sigma(R_\odot) = 0.25$, and $\sigma_{\rm RM8} = 3.6\,$kpc. The model output has been re-sampled to match the APOGEE stellar $|z|$ distribution, and a Gaussian scatter has been applied to the abundances and ages according to Table 2. The right panel plots the results from APOGEE using the Leung et al. (2023) age catalog. The contours indicate the density of stars in the [Fe/H]–[O/Fe] plane, and the vertical dashed line denotes the boundary for locally metal-rich (LMR) stars. *Bottom*: Stellar age distributions in the Solar annulus for all stars (black) and LMR stars (gray). The left and center panels plot the mass-weighted age distributions predicted by the models after forward-modeling age uncertainties, and the right panel plots the Leung et al. (2023) ages for APOGEE stars. **Key takeaway:** The two-infall model predicts a fundamentally different age pattern than what is observed, especially for LMR stars.

near $\sim 5\,$Gyr, although very few of the LMR stars have ages $\gtrsim 10\,$Gyr. Our two-infall models produce an age distribution for the overall sample that is similar to the data, but for LMR stars, both models predict a distinctly bimodal age distribution. There is a large contribution from the young, metal-rich end of the second infall, and a contribution from the old, metal-rich end of the first, but there are few stars in between. The trough between the modes lies at $\sim 5\,$Gyr for both models, right where the APOGEE distribution peaks.

Mention some ways to try to resolve this (e.g., stronger radial migration) and that they don't work. Note that our projected log age error of 0.1 dex is accurate for stars $< 8\,$Gyr old, but too large for older stars, so the scatter in the high-α sequence is larger than the data.

5. DISCUSSION

Summary of problem: the two-infall model is boxed in by data.

5.1. *Comparison with Previous Literature*

5.2. *The Empirical Yield Scale*

The $y/Z_\odot = 1$ empirical yield scale already has difficulties matching the local age–metallicity relation (Johnson et al. 2024), but the problem is exacerbated in the two-infall case because of the delayed dilution event — in effect, approach to equilibrium is "reset" by the second infall.

5.3. *Third Accretion Episode*

Motivated by evidence of a recent period of enhanced star formation (e.g., Ruiz-Lara et al. 2020), Spitoni et al. (2023) and Palla et al. (2024) extended the two-infall model with a recent third accretion episode. Spitoni et al. (2023) argued that the gas dilution resulting from the third infall could explain the population of young, metal-poor stars discovered in *Gaia* DR3 (Recio-Blanco et al. 2023), in contrast to the two-infall model of Spitoni et al. (2021) which predicted a present-day gas metallicity of [M/H] $\approx +0.3$ in the Solar neighborhood. Palla et al. (2024) were similarly motivated by the finding that open clusters with ages < 1 Gyr have similar metallicity to those with ages > 3 Gyr and younger than OCs in between, while the classical two-infall model predicted a steady increase in metallicity over time. However, Palla et al. (2024) invoke a less massive infall, producing a milder dilution event, than Spitoni et al. (2023).

Some combination of metal-rich accretion and radial gas flows might reduce the amount of dilution predicted by a recent accretion episode.

5.4. *Radial Gas Flows*

Radial gas flows are hard :'(

Some two-infall studies (e.g., Spitoni & Matteucci 2011; Palla et al. 2020, 2024) implement inward radial gas flows with velocity ~ 1 km s^{-1} in order to reproduce the radial abundance gradient without Galactic outflows.

Spitoni & Matteucci (2011) find that a two-infall model of the disk without gas exchange produces a radial metallicity gradient which is too shallow. They implement an inward radial gas flow on the order of $\sim 0-4$ km s^{-1} which varies with radius, and find that it improves agreement with the observed gradient. However, they found that a variable star formation efficiency with radius in combination with a gas density threshold for star formation could also reproduce the observed gradient without radial flows.

Radial gas flows allow GCE models to produce a radial metallicity gradient in the absence of mass-loaded outflows. We do not believe that switching from outflows to radial gas flows would solve any of our models' issues regarding the age–abundance relation, [O/Fe] distributions, or stellar age distributions.

5.5. *Star Formation Hiatus*

The two-infall model falls into the broader category of GCE models which reproduce the α-bimodality by halting or severely limiting star formation for some duration. For the two-infall model, this phase of low star formation immediately precedes the second infall epoch and is due to the relatively short timescale of the first infall epoch. However, as we have shown, the dilution of the ISM resulting from the second infall poses a challenge when comparing to age–abundance data.

A bursty infall history is not the only way to produce a gap in the star formation history. Beane et al. (2024) present a simulated galaxy from the Illustris TNG50 suite that exhibits MW-like bimodality. They argue that the α-bimodality is brought on by a brief (~ 300 Myr) quiescent period caused by bar formation. The virial mass of their galaxy grows steadily throughout this period, unlike in our two-infall model where the mass grows by a factor of X during the 1 Gyr following the second infall.

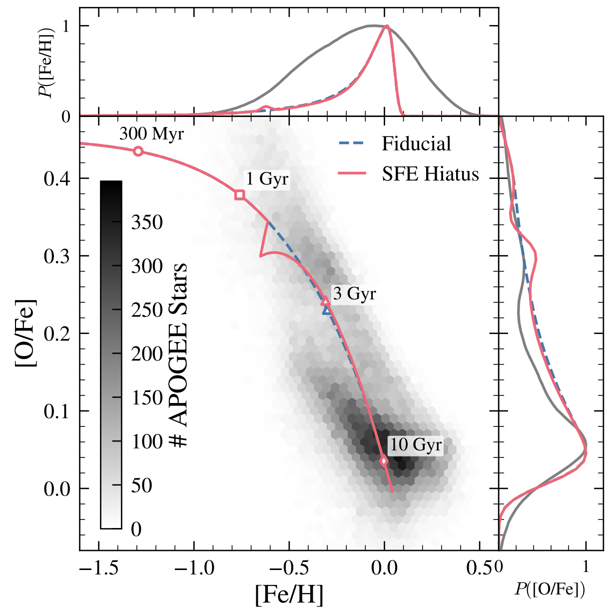

Figure 13. Abundance tracks and distributions from one-zone models which experience an efficiency-driven starburst. The blue dashed curve represents the fiducial model that has an exponentially declining infall rate and constant star formation efficiency timescale $\tau_\star = 2$ Gyr. The red solid curve plots the output of a model which experiences an enhancement of $\tau_\star$ by a factor of 10, for a duration of 200 Myr, starting at $t = 1.4$ Gyr. Both models assume the $y/Z_\odot = 2$ yield set, with $y_{\rm Fe}^{\rm Ia}$ reduced by 20% to better match the model endpoint with the data, and $\eta = 1.4$. The greyscale histogram presents the number density of APOGEE stars in the Solar annulus ($7 \leq R_{\rm gal} \leq 9$ kpc, $0 \leq |z| \leq 2$ kpc) in [O/Fe]–[Fe/H] space, and the gray histograms in the marginal panels show the APOGEE stellar abundance distributions.

While our semi-analytic model does not include a Galactic bar, we can explore the effects of a star formation hiatus by artificially boosting the SFE timescale $\tau_\star$ for a period of time. Figure 13 illustrates the effect of this SFE-driven hiatus in a one-zone model with an exponentially declining infall rate. During the quiescent period, the [O/Fe] ratio slowly declines due to the delayed contribution of Fe from SNe Ia. Meanwhile, the gas mass continues to increase even as star formation is suppressed. When $\tau_\star$ is lowered at the end of the quiescent period, the high gas mass sparks a moderate star formation burst which causes stellar abundances to "pile up" at similar [O/Fe] values. The trough between the high- and low-α sequences results from the star formation returning to pre-quiescence behavior.

Our simple hiatus model offers a few parameters which control the chemical evolution. The onset time of the SFE hiatus controls the position of the high-α sequence: a later onset places the peak at lower [O/Fe]. The duration of the star formation hiatus (and the $\tau_\star$ enhancement factor?) controls the strength of the high-α peak.

The parameters of the SFE hiatus in Figure 13 were chosen to match the APOGEE stellar [O/Fe] distribution as closely as possible. However, there are some differences in detail, such as the dearth of stars at [O/Fe] $\approx +0.35$ due to the star formation hiatus. We intend this model to illustrate another path to reproducing the α-bimodality. Most of the high-α stars present in the Solar annulus have likely migrated from the inner Galaxy, where perhaps this SFE-driven hiatus was concentrated.

6. SUMMARY & CONCLUSIONS

We have compared the predictions of the two-infall scenario against abundance data from APOGEE DR17 supplemented with age estimates using two different methods. We ran multi-zone GCE models at two different yield scales with prescriptions for radially-dependent outflows and stellar migration. While the two-infall scenario can explain the local stellar abundance distribution, in particular the α-bimodality, it faces challenges in matching the age–abundance structure of the full disk. We explored multiple parameter modifications to bring the model predictions closer to the data, including the yield scale, radial migration strength, metallicity of the accreted gas, thick-to-thin disk mass ratio, and the SN Ia DTD. Our conclusions are as follows:

- The large quantity of pristine gas accreted in the Solar neighborhood during the second infall phase rapidly dilutes the ISM metallicity by ~ 0.5 dex. Models with low nucleosynthetic yields ($y/Z_\odot = 1$) remain at sub-Solar metallicity until the present day, in stark contrast to the observed local age–metallicity relation. Models with higher yields and outflows approach the present-day metallicity more rapidly, while pre-enriched infall can reduce the magnitude of the dilution (but not eliminate it entirely).

- The "turn-over" in the evolution of [O/Fe] following the second infall produces a double-peaked low-α sequence with a fundamentally different abundance structure than observed, especially for models with higher yields. A low yield set ($y/Z_\odot = 1$) coupled with lower outflows, or pre-enrichment of the infalling gas, can bring the stellar [O/Fe] distributions more in line with the data. The parameter space is nonetheless restricted by the need to suppress this feature.

- For metal-rich stars, the two-infall model predicts a sharp divide in the stellar age distribution between the thick and thin disk populations. In contrast, the data show a smooth gradient between the oldest and youngest stars, with most of the metal-rich stars having intermediate ages.

- Our models predict that the MDF evolves to higher metallicity over time throughout the disk. This contrasts with the APOGEE data, which show very little change in the mode over the past $\sim 6-8$ Gyr.

- The equilibrium scenario of chemical evolution, if correct, places stricter limits on the two-infall model than other evolutionary models.

The apparent age-independence of stellar abundances in the disk places considerable restrictions upon the two-infall parameter space because it predicts a substantial dilution event at the start of the thin disk epoch. If the equilibrium scenario of Johnson et al. (2024) is correct, then it restricts the two-infall scenario more than other GCE models.

Implications for merger-driven SFHs.

ACKNOWLEDGEMENTS

Personal acknowledgements.

LOD and JAJ acknowledge support from National Science Foundation grant no. AST-2307621. JAJ and JWJ acknowledge support from National Science Foundation grant no. AST-1909841. LOD acknowledges financial support from an Ohio State University Fellowship. JWJ acknowledges financial support from an Ohio State University Presidential Fellowship and a Carnegie Theoretical Astrophysics Center postdoctoral fellowship. Update grants and fellowships.

Funding for the Sloan Digital Sky Survey IV has been provided by the Alfred P. Sloan Foundation, the U.S. Department of Energy Office of Science, and the Participating Institutions.

SDSS-IV acknowledges support and resources from the Center for High Performance Computing at the University of Utah. The SDSS website is www.sdss4.org.

SDSS-IV is managed by the Astrophysical Research Consortium for the Participating Institutions of the

SDSS Collaboration including the Brazilian Participation Group, the Carnegie Institution for Science, Carnegie Mellon University, Center for Astrophysics — Harvard & Smithsonian, the Chilean Participation Group, the French Participation Group, Instituto de Astrofísica de Canarias, The Johns Hopkins University, Kavli Institute for the Physics and Mathematics of the Universe (IPMU) / University of Tokyo, the Korean Participation Group, Lawrence Berkeley National Laboratory, Leibniz Institut für Astrophysik Potsdam (AIP), Max-Planck-Institut für Astronomie (MPIA Heidelberg), Max-Planck-Institut für Astrophysik (MPA Garching), Max-Planck-Institut für Extraterrestrische Physik (MPE), National Astronomical Observatories of China, New Mexico State University, New York University, University of Notre Dame, Observatário Nacional / MCTI, The Ohio State University, Pennsylvania State University, Shanghai Astronomical Observatory, United Kingdom Participation Group, Universidad Nacional Autónoma de México, University of Arizona, University of Colorado Boulder, University of Oxford, University of Portsmouth, University of Utah, University of Virginia, University of Washington, University of Wisconsin, Vanderbilt University, and Yale University.

This work has made use of data from the European Space Agency (ESA) mission *Gaia* (https://www.cosmos.esa.int/gaia), processed by the *Gaia* Data Processing and Analysis Consortium (DPAC, https://www.cosmos.esa.int/web/gaia/dpac/consortium). Funding for the DPAC has been provided by national institutions, in particular the institutions participating in the *Gaia* Multilateral Agreement.

We would like to acknowledge the land that The Ohio State University occupies is the ancestral and contemporary territory of the Shawnee, Potawatomi, Delaware, Miami, Peoria, Seneca, Wyandotte, Ojibwe and many other Indigenous peoples. Specifically, the university resides on land ceded in the 1795 Treaty of Greeneville and the forced removal of tribes through the Indian Removal Act of 1830. As a land grant institution, we want to honor the resiliency of these tribal nations and recognize the historical contexts that has and continues to affect the Indigenous peoples of this land.

Software: `VICE` (Johnson & Weinberg 2020), Astropy (Astropy Collaboration et al. 2013, 2018, 2022), scikit-learn (Pedregosa et al. 2011), SciPy (Virtanen et al. 2020), Matplotlib (Hunter 2007).

APPENDIX

A. REPRODUCIBILITY

Blah.

REFERENCES

Abdurro'uf, Accetta, K., Aerts, C., et al. 2022, The Astrophysical Journal Supplement Series, 259, 35, doi: 10.3847/1538-4365/ac4414

Asplund, M., Grevesse, N., Sauval, A. J., & Scott, P. 2009, Annual Review of Astronomy and Astrophysics, 47, 481, doi: 10.1146/annurev.astro.46.060407.145222

Astropy Collaboration, Robitaille, T. P., Tollerud, E. J., et al. 2013, Astronomy & Astrophysics, 558, A33, doi: 10.1051/0004-6361/201322068

Astropy Collaboration, Price-Whelan, A. M., Sipőcz, B. M., et al. 2018, The Astronomical Journal, 156, 123, doi: 10.3847/1538-3881/aabc4f

Astropy Collaboration, Price-Whelan, A. M., Lim, P. L., et al. 2022, The Astrophysical Journal, 935, 167, doi: 10.3847/1538-4357/ac7c74

Bailer-Jones, C. A. L., Rybizki, J., Fouesneau, M., Demleitner, M., & Andrae, R. 2021, The Astronomical Journal, 161, 147, doi: 10.3847/1538-3881/abd806

Beane, A., Johnson, J., Semenov, V., et al. 2024, Rising from the Ashes II: The Bar-driven Abundance Bimodality of the Milky Way, arXiv. http://arxiv.org/abs/2410.21580

Belokurov, V., Erkal, D., Evans, N. W., Koposov, S. E., & Deason, A. J. 2018, Monthly Notices of the Royal Astronomical Society, 478, 611, doi: 10.1093/mnras/sty982

Bennett, M., & Bovy, J. 2019, Monthly Notices of the Royal Astronomical Society, 482, 1417, doi: 10.1093/mnras/sty2813

Bensby, T., Feltzing, S., & Oey, M. S. 2014, Astronomy and Astrophysics, 562, A71, doi: 10.1051/0004-6361/201322631

Bland-Hawthorn, J., & Gerhard, O. 2016, Annual Review of Astronomy and Astrophysics, 54, 529, doi: 10.1146/annurev-astro-081915-023441

Bowen, I. S., & Vaughan, Jr., A. H. 1973, Applied Optics, 12, 1430, doi: 10.1364/AO.12.001430

Brook, C. B., Governato, F., Roškar, R., et al. 2011, Monthly Notices of the Royal Astronomical Society, 415, 1051, doi: 10.1111/j.1365-2966.2011.18545.x

Cameron, A. J., Fisher, D. B., McPherson, D., et al. 2021, The Astrophysical Journal Letters, 918, L16, doi: 10.3847/2041-8213/ac18ca

Chen, B., Hayden, M. R., Sharma, S., et al. 2023, Monthly Notices of the Royal Astronomical Society, 523, 3791, doi: 10.1093/mnras/stad1568

Chen, T., & Prantzos, N. 2025, Recent star formation episodes in the Galaxy: impact on its chemical properties and the evolution of its abundance gradient, arXiv, doi: 10.48550/arXiv.2501.03342

Chiappini, C., Matteucci, F., & Gratton, R. 1997, The Astrophysical Journal, 477, 765, doi: 10.1086/303726

Chiappini, C., Matteucci, F., & Romano, D. 2001, The Astrophysical Journal, 554, 1044, doi: 10.1086/321427

Chiappini, C., Romano, D., & Matteucci, F. 2003, Monthly Notices of the Royal Astronomical Society, 339, 63, doi: 10.1046/j.1365-8711.2003.06154.x

Chieffi, A., & Limongi, M. 2004, The Astrophysical Journal, 608, 405, doi: 10.1086/392523

Christensen, C., Quinn, T., Governato, F., et al. 2012, Monthly Notices of the Royal Astronomical Society, 425, 3058, doi: 10.1111/j.1365-2966.2012.21628.x

Conroy, C., Weinberg, D. H., Naidu, R. P., et al. 2022, Birth of the Galactic Disk Revealed by the H3 Survey, doi: 10.48550/arXiv.2204.02989

Das, S., Mathur, S., Gupta, A., & Krongold, Y. 2021, The Astrophysical Journal, 918, 83, doi: 10.3847/1538-4357/ac0e8e

Das, S., Mathur, S., Nicastro, F., & Krongold, Y. 2019, The Astrophysical Journal, 882, L23, doi: 10.3847/2041-8213/ab3b09

Dubay, L. O., Johnson, J. A., & Johnson, J. W. 2024, The Astrophysical Journal, 973, 55, doi: 10.3847/1538-4357/ad61df

Feuillet, D. K., Bovy, J., Holtzman, J., et al. 2018, Monthly Notices of the Royal Astronomical Society, 477, 2326, doi: 10.1093/mnras/sty779

Frankel, N., Rix, H.-W., Ting, Y.-S., Ness, M., & Hogg, D. W. 2018, The Astrophysical Journal, 865, 96, doi: 10.3847/1538-4357/aadba5

François, P., Matteucci, F., Cayrel, R., et al. 2004, Astronomy & Astrophysics, 421, 613, doi: 10.1051/0004-6361:20034140

Fuhrmann, K. 1998, Astronomy and Astrophysics, 338, 161. https://ui.adsabs.harvard.edu/abs/1998A&A...338..161F

Fuhrmann, K., Chini, R., Kaderhandt, L., & Chen, Z. 2017, Monthly Notices of the Royal Astronomical Society, 464, 2610, doi: 10.1093/mnras/stw2526

Gaia Collaboration, Prusti, T., de Bruijne, J. H. J., et al. 2016, Astronomy and Astrophysics, 595, A1, doi: 10.1051/0004-6361/201629272

Gaia Collaboration, Brown, A. G. A., Vallenari, A., et al. 2021, Astronomy and Astrophysics, 649, A1, doi: 10.1051/0004-6361/202039657

Gallart, C., Bernard, E. J., Brook, C. B., et al. 2019, Nature Astronomy, 3, 932, doi: 10.1038/s41550-019-0829-5

García Pérez, A. E., Allende Prieto, C., Holtzman, J. A., et al. 2016, The Astronomical Journal, 151, 144, doi: 10.3847/0004-6256/151/6/144

Gilmore, G., & Reid, N. 1983, Monthly Notices of the Royal Astronomical Society, 202, 1025, doi: 10.1093/mnras/202.4.1025

GRAVITY Collaboration, Abuter, R., Amorim, A., et al. 2018, Astronomy and Astrophysics, 615, L15, doi: 10.1051/0004-6361/201833718

Griffith, E. J., Sukhbold, T., Weinberg, D. H., et al. 2021, The Astrophysical Journal, 921, 73, doi: 10.3847/1538-4357/ac1bac

Gunn, J. E., Siegmund, W. A., Mannery, E. J., et al. 2006, The Astronomical Journal, 131, 2332, doi: 10.1086/500975

Gupta, A., Kingsbury, J., Mathur, S., et al. 2021, The Astrophysical Journal, 909, 164, doi: 10.3847/1538-4357/abdbb6

Gutcke, T. A., Stinson, G. S., Macciò, A. V., Wang, L., & Dutton, A. A. 2017, Monthly Notices of the Royal Astronomical Society, 464, 2796, doi: 10.1093/mnras/stw2539

Hayden, M. R., Bovy, J., Holtzman, J. A., et al. 2015, The Astrophysical Journal, 808, 132, doi: 10.1088/0004-637X/808/2/132

Helmi, A., Babusiaux, C., Koppelman, H. H., et al. 2018, Nature, 563, 85, doi: 10.1038/s41586-018-0625-x

Holtzman, J. A., Shetrone, M., Johnson, J. A., et al. 2015, The Astronomical Journal, 150, 148, doi: 10.1088/0004-6256/150/5/148

Howell, D. A., Sullivan, M., Brown, E. F., et al. 2009, The Astrophysical Journal, 691, 661, doi: 10.1088/0004-637X/691/1/661

Hu, C.-Y., Smith, M. C., Teyssier, R., et al. 2023, The Astrophysical Journal, 950, 132, doi: 10.3847/1538-4357/accf9e

Hunter, J. D. 2007, Computing in Science & Engineering, 9, 90, doi: 10.1109/MCSE.2007.55

Iben, Jr., I. 1967, Annual Review of Astronomy and Astrophysics, 5, 571, doi: 10.1146/annurev.aa.05.090167.003035

Iwamoto, K., Brachwitz, F., Nomoto, K., et al. 1999, The Astrophysical Journal Supplement Series, 125, 439, doi: 10.1086/313278

Johnson, J. W., & Weinberg, D. H. 2020, Monthly Notices of the Royal Astronomical Society, 498, 1364, doi: 10.1093/mnras/staa2431

Johnson, J. W., Weinberg, D. H., Vincenzo, F., et al. 2021, Monthly Notices of the Royal Astronomical Society, 508, 4484, doi: 10.1093/mnras/stab2718

Johnson, J. W., Weinberg, D. H., Blanc, G. A., et al. 2024, The Milky Way Radial Metallicity Gradient as an Equilibrium Phenomenon: Why Old Stars are Metal-Rich, doi: 10.48550/arXiv.2410.13256

Jurić, M., Ivezić, , Brooks, A., et al. 2008, The Astrophysical Journal, 673, 864, doi: 10.1086/523619

Jönsson, H., Holtzman, J. A., Allende Prieto, C., et al. 2020, The Astronomical Journal, 160, 120, doi: 10.3847/1538-3881/aba592

Kennicutt, Jr., R. C. 1998, The Astrophysical Journal, 498, 541, doi: 10.1086/305588

Kobayashi, C., Bhattacharya, S., Arnaboldi, M., & Gerhard, O. 2023, The Astrophysical Journal, 956, L14, doi: 10.3847/2041-8213/acf7c7

Kopenhafer, C., O'Shea, B. W., & Voit, G. M. 2023, The Astrophysical Journal, 951, 107, doi: 10.3847/1538-4357/accbb7

Kubryk, M., Prantzos, N., & Athanassoula, E. 2015, Astronomy and Astrophysics, 580, A126, doi: 10.1051/0004-6361/201424171

Lehmann, C., Feltzing, S., Feuillet, D., & Kordopatis, G. 2024, Monthly Notices of the Royal Astronomical Society, 533, 538, doi: 10.1093/mnras/stae1736

Leroy, A. K., Walter, F., Brinks, E., et al. 2008, The Astronomical Journal, 136, 2782, doi: 10.1088/0004-6256/136/6/2782

Leung, H. W., Bovy, J., Mackereth, J. T., & Miglio, A. 2023, Monthly Notices of the Royal Astronomical Society, 522, 4577, doi: 10.1093/mnras/stad1272

Li, H., Vogelsberger, M., Marinacci, F., Sales, L. V., & Torrey, P. 2020, Monthly Notices of the Royal Astronomical Society, 499, 5862, doi: 10.1093/mnras/staa3122

Licquia, T. C., & Newman, J. A. 2015, The Astrophysical Journal, 806, 96, doi: 10.1088/0004-637X/806/1/96

Limongi, M., & Chieffi, A. 2006, The Astrophysical Journal, 647, 483, doi: 10.1086/505164

Lopez, L. A., Mathur, S., Nguyen, D. D., Thompson, T. A., & Olivier, G. M. 2020, The Astrophysical Journal, 904, 152, doi: 10.3847/1538-4357/abc010

Lopez, S., Lopez, L. A., Nguyen, D. D., et al. 2023, The Astrophysical Journal, 942, 108, doi: 10.3847/1538-4357/aca65e

Lu, Y. L., Minchev, I., Buck, T., et al. 2024, Monthly Notices of the Royal Astronomical Society, 535, 392, doi: 10.1093/mnras/stae2364

Mackereth, J. T., Crain, R. A., Schiavon, R. P., et al. 2018, Monthly Notices of the Royal Astronomical Society, 477, 5072, doi: 10.1093/mnras/sty972

Mackereth, J. T., Bovy, J., Schiavon, R. P., et al. 2017, Monthly Notices of the Royal Astronomical Society, 471, 3057, doi: 10.1093/mnras/stx1774

Mackereth, J. T., Bovy, J., Leung, H. W., et al. 2019, Monthly Notices of the Royal Astronomical Society, 489, 176, doi: 10.1093/mnras/stz1521

Majewski, S. R., Schiavon, R. P., Frinchaboy, P. M., et al. 2017, The Astronomical Journal, 154, 94, doi: 10.3847/1538-3881/aa784d

Maoz, D., & Graur, O. 2017, The Astrophysical Journal, 848, 25, doi: 10.3847/1538-4357/aa8b6e

Maoz, D., & Mannucci, F. 2012, Publications of the Astronomical Society of Australia, 29, 447, doi: 10.1071/AS11052

Mathur, S. 2022, in Handbook of X-ray and Gamma-ray Astrophysics, 59, doi: 10.1007/978-981-16-4544-0_112-1

Matteucci, F., & Greggio, L. 1986, Astronomy and Astrophysics, 154, 279. https://ui.adsabs.harvard.edu/abs/1986A&A...154..279M/abstract

Matteucci, F., Spitoni, E., Recchi, S., & Valiante, R. 2009, Astronomy and Astrophysics, 501, 531, doi: 10.1051/0004-6361/200911869

Mazzali, P. A., Röpke, F. K., Benetti, S., & Hillebrandt, W. 2007, Science, 315, 825, doi: 10.1126/science.1136259

Melioli, C., Brighenti, F., D'Ercole, A., & de Gouveia Dal Pino, E. M. 2008, Monthly Notices of the Royal Astronomical Society, 388, 573, doi: 10.1111/j.1365-2966.2008.13446.x

—. 2009, Monthly Notices of the Royal Astronomical Society, 399, 1089, doi: 10.1111/j.1365-2966.2009.14725.x

Minchev, I., Chiappini, C., & Martig, M. 2013, Astronomy and Astrophysics, 558, A9, doi: 10.1051/0004-6361/201220189

Myers, N., Donor, J., Spoo, T., et al. 2022, The Astronomical Journal, 164, 85, doi: 10.3847/1538-3881/ac7ce5

Méndez-Delgado, J. E., Amayo, A., Arellano-Córdova, K. Z., et al. 2022, Monthly Notices of the Royal Astronomical Society, 510, 4436, doi: 10.1093/mnras/stab3782

Naidu, R. P., Conroy, C., Bonaca, A., et al. 2021, The Astrophysical Journal, 923, 92, doi: 10.3847/1538-4357/ac2d2d

Nataf, D. M., Schlaufman, K. C., Reggiani, H., & Hahn, I. 2024, Accurate, Precise, and Physically Self-consistent Ages and Metallicities for 400,000 Solar Neighborhood Subgiant Branch Stars, arXiv, doi: 10.48550/arXiv.2407.18307

Nelson, D., Pillepich, A., Springel, V., et al. 2019, Monthly Notices of the Royal Astronomical Society, 490, 3234, doi: 10.1093/mnras/stz2306

Nidever, D. L., Holtzman, J. A., Allende Prieto, C., et al. 2015, The Astronomical Journal, 150, 173, doi: 10.1088/0004-6256/150/6/173

Nidever, D. L., Gilbert, K., Tollerud, E., et al. 2024, in , eprint: arXiv:2306.04688, 115–122, doi: 10.1017/S1743921323002016

Nissen, P. E., Christensen-Dalsgaard, J., Mosumgaard, J. R., et al. 2020, Astronomy and Astrophysics, 640, A81, doi: 10.1051/0004-6361/202038300

Palicio, P. A., Spitoni, E., Recio-Blanco, A., et al. 2023, Analytic solution of Chemical Evolution Models with Type Ia SNe, arXiv, doi: 10.48550/arXiv.2304.00042

Palla, M., Magrini, L., Spitoni, E., et al. 2024, Astronomy & Astrophysics, 690, A334, doi: 10.1051/0004-6361/202451395

Palla, M., Matteucci, F., Spitoni, E., Vincenzo, F., & Grisoni, V. 2020, Monthly Notices of the Royal Astronomical Society, 498, 1710, doi: 10.1093/mnras/staa2437

Palla, M., Santos-Peral, P., Recio-Blanco, A., & Matteucci, F. 2022, Astronomy and Astrophysics, 663, A125, doi: 10.1051/0004-6361/202142645

Parul, H., Bailin, J., Loebman, S. R., et al. 2025, Effect of gas accretion on α-element bimodality in Milky Way-mass galaxies in the FIRE-2 simulations, arXiv, doi: 10.48550/arXiv.2501.12342

Pedregosa, F., Varoquaux, G., Gramfort, A., et al. 2011, Journal of Machine Learning Research, 12, 2825. http://jmlr.org/papers/v12/pedregosa11a.html

Peschken, N., Hanasz, M., Naab, T., Wółtański, D., & Gawryszczak, A. 2021, Monthly Notices of the Royal Astronomical Society, 508, 4269, doi: 10.1093/mnras/stab2784

Pinsonneault, M. H., Zinn, J. C., Tayar, J., et al. 2025, The Astrophysical Journal Supplement Series, 276, 69, doi: 10.3847/1538-4365/ad9fef

Prantzos, N., Abia, C., Chen, T., et al. 2023, Monthly Notices of the Royal Astronomical Society, 523, 2126, doi: 10.1093/mnras/stad1551

Ratcliffe, B., Minchev, I., Anders, F., et al. 2023, Monthly Notices of the Royal Astronomical Society, 525, 2208, doi: 10.1093/mnras/stad1573

Recio-Blanco, A., Kordopatis, G., Laverny, P. d., et al. 2023, Astronomy & Astrophysics, 674, A38, doi: 10.1051/0004-6361/202243511

Rodríguez, , Maoz, D., & Nakar, E. 2023, The Astrophysical Journal, 955, 71, doi: 10.3847/1538-4357/ace2bd

Romano, D., Matteucci, F., Salucci, P., & Chiappini, C. 2000, The Astrophysical Journal, 539, 235, doi: 10.1086/309223

Ruiz-Lara, T., Gallart, C., Bernard, E. J., & Cassisi, S. 2020, Nature Astronomy, 4, 965, doi: 10.1038/s41550-020-1097-0

Schönrich, R., & Binney, J. 2009, Monthly Notices of the Royal Astronomical Society, 396, 203, doi: 10.1111/j.1365-2966.2009.14750.x

Sellwood, J. A., & Binney, J. J. 2002, Monthly Notices of the Royal Astronomical Society, 336, 785, doi: 10.1046/j.1365-8711.2002.05806.x

Sharma, S., Hayden, M. R., & Bland-Hawthorn, J. 2021, Monthly Notices of the Royal Astronomical Society, 507, 5882, doi: 10.1093/mnras/stab2015

Siegel, M. H., Majewski, S. R., Reid, I. N., & Thompson, I. B. 2002, The Astrophysical Journal, 578, 151, doi: 10.1086/342469

Spitoni, E., Cescutti, G., Minchev, I., et al. 2019, Astronomy and Astrophysics, 628, A38, doi: 10.1051/0004-6361/201834665

Spitoni, E., & Matteucci, F. 2011, Astronomy and Astrophysics, 531, A72, doi: 10.1051/0004-6361/201015749

Spitoni, E., Matteucci, F., Gratton, R., et al. 2024, Astronomy & Astrophysics, 690, A208, doi: 10.1051/0004-6361/202450754

Spitoni, E., Matteucci, F., Recchi, S., Cescutti, G., & Pipino, A. 2009, Astronomy and Astrophysics, 504, 87, doi: 10.1051/0004-6361/200911768

Spitoni, E., Recchi, S., & Matteucci, F. 2008, Astronomy and Astrophysics, 484, 743, doi: 10.1051/0004-6361:200809403

Spitoni, E., Romano, D., Matteucci, F., & Ciotti, L. 2015, The Astrophysical Journal, 802, 129, doi: 10.1088/0004-637X/802/2/129

Spitoni, E., Verma, K., Silva Aguirre, V., & Calura, F. 2020, Astronomy and Astrophysics, 635, A58, doi: 10.1051/0004-6361/201937275

Spitoni, E., Verma, K., Silva Aguirre, V., et al. 2021, Astronomy and Astrophysics, 647, A73, doi: 10.1051/0004-6361/202039864

Spitoni, E., Recio-Blanco, A., de Laverny, P., et al. 2023, Astronomy and Astrophysics, 670, A109, doi: 10.1051/0004-6361/202244349

Sukhbold, T., Ertl, T., Woosley, S. E., Brown, J. M., & Janka, H. T. 2016, The Astrophysical Journal, 821, 38, doi: 10.3847/0004-637X/821/1/38

Sánchez, S. F. 2020, Annual Review of Astronomy and Astrophysics, 58, 99, doi: 10.1146/annurev-astro-012120-013326

Thompson, T. A., & Heckman, T. M. 2024, Annual Review of Astronomy and Astrophysics, 62, 529, doi: 10.1146/annurev-astro-041224-011924

Tinsley, B. M. 1979, The Astrophysical Journal, 229, 1046, doi: 10.1086/157039

Tumlinson, J., Peeples, M. S., & Werk, J. K. 2017, Annual Review of Astronomy and Astrophysics, 55, 389, doi: 10.1146/annurev-astro-091916-055240

Veilleux, S., Maiolino, R., Bolatto, A. D., & Aalto, S. 2020, The Astronomy and Astrophysics Review, 28, 2, doi: 10.1007/s00159-019-0121-9

Vincenzo, F., Matteucci, F., Belfiore, F., & Maiolino, R. 2016, Monthly Notices of the Royal Astronomical Society, 455, 4183, doi: 10.1093/mnras/stv2598

Virtanen, P., Gommers, R., Oliphant, T. E., et al. 2020, Nature Methods, 17, 261, doi: 10.1038/s41592-019-0686-2

Weinberg, D. H., Andrews, B. H., & Freudenburg, J. 2017, The Astrophysical Journal, 837, 183, doi: 10.3847/1538-4357/837/2/183

Weinberg, D. H., Griffith, E. J., Johnson, J. W., & Thompson, T. A. 2024, The Astrophysical Journal, 973, 122, doi: 10.3847/1538-4357/ad6313

Wilson, J. C., Hearty, F. R., Skrutskie, M. F., et al. 2019, Publications of the Astronomical Society of the Pacific, 131, 055001, doi: 10.1088/1538-3873/ab0075

Woody, T., Conroy, C., Cargile, P., et al. 2025, The Astrophysical Journal, 978, 152, doi: 10.3847/1538-4357/ad968e

Woosley, S. E., & Weaver, T. A. 1995, The Astrophysical Journal Supplement Series, 101, 181, doi: 10.1086/192237